

Large-scale structure of the Universe. The Zeldovich approximation and the adhesion model

S N Gurbatov, A I Saichev, S F Shandarin

DOI: 10.3367/UFNe.0182.201203a.0233

Contents

1. Introduction	223
2. Basic formation laws of the large-scale structure of the Universe	225
3. Equations for the gas of gravitationally interacting particles	227
4. The Zeldovich approximation	228
4.1 Basic equations; 4.2 The modified Zeldovich approximation; 4.3 Lagrangian and Eulerian statistics of matter; 4.4 Statistics of flows and matter density distribution; 4.5 Spectrum of density fluctuations	
5. The adhesion model	235
5.1 From the Zeldovich model to the adhesion model; 5.2 Calculation of density in the adhesion model, finite viscosity; 5.3 The general and asymptotic solutions of the vector Burgers equation; 5.4 Flows of locally interacting particles and a singular density field; 5.5 The web-like structure in the adhesion model; 5.6 Particle dynamics inside velocity field discontinuities in the Hamilton–Jacobi equation	
6. Statistical properties of the potential turbulence: the Burgers vector turbulence	245
7. Conclusion	247
References	248

Abstract. A semianalytic formation model for the large-scale structure of the Universe (from a few to hundreds of megaparsecs) is discussed. The model is a natural generalization of Zeldovich’s 1970 approximation and is mathematically based on the Burgers equation for low or even vanishing viscosity. It offers a natural explanation of the galaxy distribution that is observed in the scale range mentioned above and is reminiscent in its shape of a 3D mosaic or a giant cosmic web. Many predictions of the model have been confirmed by modern observations. New theoretical results related to the Burgers model are discussed together with their applications to cosmology.

1. Introduction

Forty years ago, Zeldovich published two related papers discussing the question of the large-scale structure of the Universe: one in Russian in *Astrofizika* [1] and the other in English in the European journal *Astronomy and Astro-*

physics [2]. The fate of both papers was difficult: in the first 20 years, there were only 33 and 200 references to the Russian and English papers, respectively. The citation rate increased in the next 20 years: the Russian paper was cited 74 times and the English, 950 times, which made it one of the most cited papers published in *Astronomy and Astrophysics* over the 40 years of its existence [3]. In addition, an uncounted number of authors have just referred to the Zeldovich approximation without giving any reference.

In papers [1, 2], Zeldovich, with his customary easiness and clarity of thinking, introduced the culinary term ‘pancake’ into cosmology, which became very popular in the cosmological literature. The aim of the present review is to develop the ‘pancake idea’ and to show its role in the modern theory of the large-scale structure of the Universe.

The large-scale structure of the Universe has been discussed many times in *Physics–Uspekhi*. In particular, reviews with similar titles were published in 1983 [4] and 1995 [5]. One and a half decade after the publication of review [5], the situation in cosmology significantly changed once again, although not so radically as after 1983. From the standpoint of the topic under discussion, the most significant changes can be summarized as follows.

- Starting from 1998, observations of remote supernovae (SNs) have increasingly evidenced the accelerated expansion of the Universe [6, 7].

- Most cosmologists believe that dark energy, which makes up three fourths of the total energy density in the Universe, can explain these observations (see, e.g., [8, 9]).

- The joint analysis of multi-year observations of the cosmic microwave background anisotropy (the Wilkinson Microwave Background Probe, WMAP) [10] and the results of two completed, large programs of galaxy redshift measure-

S N Gurbatov, A I Saichev Department of Radiophysics,
Lobachevsky Nizhny Novgorod State University,
prosp. Gagarina 23, 603950 Nizhny Novgorod, Russian Federation
E-mail: gurb@rf.unn.ru, saichev@hotmail.com
S F Shandarin Department of Physics and Astronomy,
University of Kansas,
1082 Malott, 1251 Wescoe Hall Dr., Lawrence, KS 66045-7582, USA
E-mail: sergei@ku.edu

Received 29 April 2011, revised 26 September 2011

Uspekhi Fizicheskikh Nauk 182 (3) 233–261 (2012)

DOI: 10.3367/UFNr.0182.201203a.0233

Translated by K A Postnov; edited by A M Semikhatov

ments, the Two-degree-Field Galaxy Redshift Survey (2DF) [11] and the Sloan Digital Sky Survey (SDSS) [12], allowed significant improvement in measurements of the main cosmological parameters of the Universe.

- The Hubble constant, which characterizes the present expansion rate of the Universe, was measured most reliably from the analysis of data obtained in the Hubble Space Telescope Key Project [13].

The main cosmological parameters, from our standpoint, were obtained from a joint analysis of all relevant data, including the WMAP5 results, observations of Baryon acoustic oscillations (BAOs), and measurements of distant supernovae [14]. For the convenience of the reader, the cosmological parameters are listed in Table 1. We only briefly explain the physical meaning of each of them. For more a detailed discussion of the role of these parameters, we recommend the book by Gorbunov and Rubakov [8], two recent reviews in *Physics–Uspekhi* [15, 16], and paper [14].

Table 1. Basic cosmological parameters.

Parameter	Value
h	0.705 ± 0.013
Ω_A	0.726 ± 0.015
$\Omega_{\text{CDM}}h^2$	0.113 ± 0.003
$\Omega_b h^2$	0.0227 ± 0.0006
$\Omega_m h^2$	0.136 ± 0.004
n	0.960 ± 0.013
σ_8	0.81 ± 0.03

The Hubble constant H_0 determining the present-day rate of expansion of the Universe is traditionally given as the dimensional parameter $h = H_0/[100 \text{ km (s Mpc)}^{-1}]$. The parameters Ω_A , Ω_{CDM} , Ω_b , and Ω_m respectively denote the dark energy density, the mean density of dark matter and ordinary baryon matter, and the sum of all nonrelativistic mass components in units of the critical density $\rho_c \equiv 3H_0^2/(8\pi G) \approx 1.88 \times 10^{-29} h^2 \text{ g cm}^{-3}$, where G is the Newton gravitational constant. The parameters n and σ_8 respectively characterize the shape and normalization of the spectrum of initial perturbations.

The physical role of these parameters is explained below. Nevertheless, we now wish to stress an increased precision of measurements of cosmological parameters at the level of one to two percent. Overall, the cosmological model is currently known much better than 15 years ago. Therefore, parameters of the large-scale structure and the most important aspects of its formation, which directly depend on the cosmological model, can be described by the theory with much better accuracy.

Both observational and theoretical studies of the large-scale structure of the Universe have significantly increased in the last two decades, especially in relating numerical simulations to theory, as most observational astronomer believe. However, we believe that numerical modeling is close in spirit to the work of an experimental physicist. Similarly to a physical experiment, conditions that are simpler than in nature are created in numerical models, which allows studying them analytically in greater detail.

The principal task of this review is to consider analytic models proposed to describe the structure of the Universe on

large scales exceeding 1 Mpc. In particular, special attention is given to the complex geometry and topology of the structure, which were suggested for the first time within the Zeldovich approximation (ZA), but were denied by most leading theoreticians from the USA and other western countries for 15–20 years [3] after the publication of Zeldovich's papers [1, 2].

The main feature distinguishing the present review from reviews [4, 5] is that we consider the so-called standard cosmological model, or the Λ CDM (Lambda-Cold Dark Matter) model, which differs from both the HDM (Hot Dark Matter) model assumed in [4] and the CDM (Cold Dark Matter) model considered in [5]. In addition, review [5] focuses on the central structure of virialized halos, whose density profiles were proposed by the authors as being described by an analytic solution, while here we primarily study the global picture of the large-scale structure, i.e., the formation of filaments and their role in integrating the halos into a unique connected structure called the cosmic web or cosmic net. This by no means implies that the properties of dark matter halos are less interesting. Not at all—the significant difference between the results of modern numerical modeling of halos using a record large number of particles (4.4 bln) [17] and theoretical predictions [5] already deserves a thorough analysis; however, this problem is beyond the scope of this review and should be discussed separately.

The so-called adhesion model (AM) is a comparatively simple but at the same time effective analytic approximation describing the formation and evolution of the large-scale structure of matter distribution in the Universe. The adhesion model is based on the ZA and reproduces the main geometrical features of the observed galaxy distribution structure on scales from 1 Mpc to several hundred Mpc both qualitatively and quantitatively.

The AM involves a nonlinear diffusion equation, the multidimensional Burgers equation (BE). The well-known general solution of the BE allows detailed studies of the large-scale structure behavior in the framework of the AM. The limit form of the AM corresponding to a vanishing viscosity coefficient in the BE leads to the formation of an irregular mosaic structure, which can be treated as a geometrical skeleton of matter distribution in the Universe.

The typical elements of the mosaic structure — vertices, edges, faces, and individual cells — can be associated with different types of astronomical objects, such as galaxy clusters and superclusters and huge dark voids between them, where the density of galaxies is very low [18]. Currently, the vertices of the mosaic large-scale structure correspond to galaxy clusters. Quasi-1D filaments of galaxies corresponding to edges of the mosaic structure, which represent another typical element of the large-scale structure, contain a small mass fraction of the Universe. At the same time, faces of the cells contain a small amount of mass and, in addition, have a low density contrast, and are therefore the most difficult to recognize. The identification of the structure elements is a difficult and still unsolved problem of cosmology, whence the uncertainty in their geometry and mass determination. For example, a recent numerical calculation of the structure in the standard cosmological model showed that most mass (about 39%) is contained in edges (filaments), the vertices (clusters) comprise about 28% of matter, somewhat more than 27% of matter is inside the cells, and the least amount of dark

matter resides in faces (less than 6%) [19]. We emphasize that the results of such calculations obtained by different groups depend on the adopted identification algorithm of the structure elements, as well as on the spatial resolution of the model, and can therefore be significantly different.

The evolution of the large-scale structure of the Universe itself can be treated as a continuous process of matter transport predominantly from objects with a high dimension to those with a mosaic structure, which have a lower dimension. For example, matter flows from the inner cells of the mosaic structure (3D objects) to its faces (quasi-2D objects), and from them to the edges and vertices of the mosaic structure. At the same time, there is a continuous motion, deformation, and merging of cells [20]. Recently, similar conclusions were obtained by a group of researchers from Princeton University (USA), who studied the galaxy distribution using SDSS [21, 22].

All these formation features of the large-scale structure of the Universe are considered in this review using various approaches that are now generally accepted: the ZA, the numerical modeling of N gravitationally interacting particles, and the AM. The results of these approaches are analyzed and compared. It is shown that the adhesion approximation is the most convenient analytic tool for studying the large-scale structure and is in good agreement with both the results of other approaches and cosmological observations.

The structure of the review is as follows. In Section 2, we provide basic facts about the large-scale structure of matter in the Universe, known from cosmological observations and physical principles. The main focus is on the role of dark matter in the large-scale structure formation. In Section 3, equations describing the evolution of density inhomogeneities in the Universe are formulated. Sections 4 and 5 describe the appearance and evolution of structure in the framework of the ZA and AM; in particular, similarities and differences of these approaches are discussed. In Section 6, we briefly discuss statistical characteristics of the potential turbulence, the vector Burgers turbulence.

2. Basic formation laws of the large-scale structure of the Universe

We are living in an expanding Universe, as was theoretically predicted in 1922 by Russian mathematician A Friedman [23]. In 1929, American astronomer E Hubble [24] independently discovered the expansion of the Universe.

We explain the essence of the expansion of the Universe with the example of an idealized Universe that is homogeneous everywhere. The expansion of the Universe means that any two particles located at a distance \mathbf{r} from each other move away along the direct line connecting their centers with a relative velocity \mathbf{u} that follows the Hubble law:

$$\mathbf{u} = H(t) \mathbf{r}. \quad (1)$$

In the real inhomogeneous Universe, law (1) is approximately valid only at large distances between the particles. The positive factor $H(t)$ is called the Hubble parameter, and its present-day value is called the Hubble constant. The Hubble parameter quantitatively characterizes the expansion rate of the Universe. Presently, the expansion rate of the Universe is $H_0 = H(t_0) = 100h \approx 70.5 \text{ km s}^{-1} \text{ Mpc}^{-1}$ (1 Mpc = $10^6 \text{ pc} \approx 3,260,000 \text{ light years}$) (see Table 1).

Until the end of the 20th century, most cosmologists believed that the expansion rate of the Universe was larger in the past and monotonically decreased with time (i.e., $\dot{H} < 0$ for any $t > 0$) due to gravitational attraction. But the study of motion of very distant supernovae showed that the expansion of the Universe has recently (on a cosmological time scale) started accelerating [6, 7].

The acceleration of the expansion of the Universe can be quite simply explained by assuming that most of the Universe is filled with dark energy—a hypothetical substance uniformly distributed in space. Although the nature of dark energy is still unknown, the most popular current explanation of the accelerated expansion of the Universe assumes the existence of dark energy. According to this hypothesis, dark energy has an equation of state that is unusual for ordinary matter, $p = -\varepsilon$, where p is the pressure and ε is the energy density. The negative sign of the pressure causes the accelerated expansion of the Universe. The equation of state given above corresponds to the simplest model of dark energy and the presence of the cosmological constant term in the Einstein equations (see, e.g., [8, 9]).

Although dark matter particles have not yet been found in physical experiments, the hypothesis of dark matter is firmly justified. Gravitational interaction of dark matter particles is similar to that of ordinary matter particles. Because of its dominance over ordinary matter in the gravitational interaction force, dark matter plays the decisive role in the formation and evolution of the large-scale structure of the Universe.

It is well known that the Universe is permeated by the cosmic microwave background radiation (CMB), which carries unique information on the properties of the Universe as a whole (which are characterized by the values of cosmological parameters) as well as on small initial deviations of the matter density in the Universe from a smooth uniform distribution; these initial perturbations served as the ‘seeds’ of the structure of the Universe presently observed. We know from the analysis of CMB that with a high accuracy, the seeding fluctuation density field is represented by a realization of the random Gaussian field whose power density can be reliably determined from CMB measurements.

As can be seen from Fig. 1, the present-day Universe is inhomogeneous on scales up to several hundred megaparsecs.

We note, however, that Fig. 1 does not correctly represent the actual distribution of galaxies in physical space, because the locations of points (symbolizing galaxies) are obtained by a recalculation of galaxy velocities in their coordinates using Hubble law (1). In an inhomogeneous Universe, the true relation between the distance r and the observed radial velocity u_{obs} should be given by

$$u_{\text{obs}} = H_0 r + u_p, \quad (2)$$

including the additional term u_p that is called the peculiar velocity and appears because of the density inhomogeneity in the Universe due to the motion of particles relative to the homogeneous expansion. The total radial velocity component u_{obs} can be measured using the Doppler effect, while measuring the peculiar velocity vector \mathbf{u}_p is impossible. We can roughly estimate its radial component u_p only on spatial scales not exceeding the distance to several thousand nearby bright galaxies, which is too small for studying the geometry of the large-scale structure of the Universe. Therefore, distances to galaxies derived from observations of their

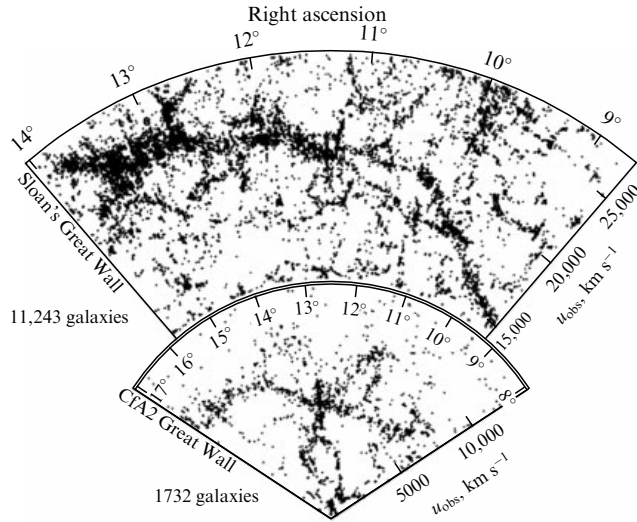


Figure 1. Two examples of galaxy distribution in the Universe. Scales shown in velocity units (km s^{-1}) can be converted into megaparsecs using Hubble law (1). Each point corresponds to a galaxy [25, 26].

radial velocities,

$$r_{\text{est}} = \frac{u_{\text{obs}}}{H_0} = r + \frac{u_p}{H_0},$$

give only a rough estimate of their actual values, which introduces a serious bias in the geometry and scales of the real physical structure.

The matter density distribution in the Universe can be illustrated most clearly (in some statistical sense) by numerically simulating the motion of N gravitationally interacting particles in the framework of the standard model (the N -body problem). The result of such a simulation is shown in Fig. 2 [27].

In cosmology, the notion of the large-scale structure is related to distributions of galaxies and dark matter on scales from 1 Mpc to several hundred megaparsecs. On smaller scales, the effect of discreteness of galaxy distribution becomes important, while on large scales, the distributions monotonically tend to homogeneous ones. Redshift observa-

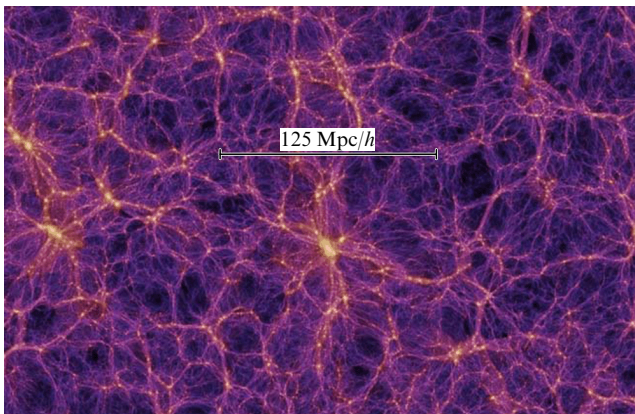


Figure 2. Dark matter density field in the Universe obtained in numerical simulations of the large-scale structure formation. Dark areas in this figure correspond to low-density regions, light areas show high-density large-scale structures [27].

tions reveal different structures that are usually characterized as filaments or mosaic structures [21, 22, 25, 26] and can be clearly seen in Figs 1 and 2.

We emphasize once again that the process of the emergence of the large-scale structure is one of the important issues in cosmology. Many fundamental questions of physics, cosmology, and astronomy, such as the explanation of the physical nature of dark matter, measurement of the angular anisotropy of CMB, and the determination of the galaxy formation epoch are tightly related to the question of the appearance and formation of the large-scale structure of the Universe (see, e.g., [28–31]).

Modern theory explains the formation of the large-scale structure of the Universe as a consequence of the increase in the initially small matter density fluctuations due to gravitational instability [32, 33]. It is assumed that the initial density fluctuations appear as vacuum fluctuations at the very early stage of the evolution of the Universe, when the Universe was expanding exponentially, in the epoch of the so-called inflationary Universe (see, e.g., [9]). These initial density fluctuations passed a long way before they gave rise to the formation of galaxies, galaxy clusters, superclusters, and voids. The galaxy formation problem is very complicated in and of itself. Many extremely complex physical processes, such as star formation and supernova explosions, are fundamentally important for understanding galaxy formation. We do not discuss these complicated processes and focus on the matter distribution in the Universe in the rough large-scale approximation, according to which galaxies can be considered ‘elementary’ particles (point masses), which is justified by the small sizes of galaxies relative to the size of galaxy clusters and superclusters, not to mention huge dark void volumes.

As long as matter density fluctuations in the Universe are small, their evolution can be well described by the linear theory of gravitational instability (see, e.g., [28–31]). The linear theory of gravitational instability is quite simple and admits a clear interpretation. Notably, this theory predicts that the growth rate of density perturbations $D(t)$ is

$$D(t) \propto \delta, \quad (3)$$

where $\delta \equiv \delta\rho/\bar{\rho}$ and $\delta\rho = \rho - \bar{\rho}$ is the matter density fluctuations. In the linear theory, the normalization of the function $D(t)$ is arbitrary, and can therefore be chosen conveniently. We recall that the linear approximation is valid as long as the inequality $\sqrt{\langle\delta^2\rangle} \ll 1$ holds.

At the nonlinear stage of the gravitational instability, $\sqrt{\langle\delta^2\rangle} \gtrsim 1$, when density perturbations become large and the large-scale structure starts emerging (sheets, filaments, and compact clusters of galaxies), the description of the evolution of density fluctuations in Eulerian coordinates becomes very complicated.

The most obvious way to account for the complexity of the nonlinear gravitational instability effect on the matter density field evolution is by numerical simulation of the 3D N -body problem (see, e.g., [34, 35] and Fig. 2). The relevance of such a simulation agrees with the hypothesis that dark matter consists of particles interacting only gravitationally. In the simulation, the trajectory of an individual particle is calculated by numerical integration of the equations of motion in the gravitational field created by other particles. To imitate the boundlessness of the Universe, periodic initial conditions are posed.

Below, we discuss other approaches to the description of the large-scale structure of the Universe; namely, we consider in some detail two approximate analytic solutions of some partial differential equations that correctly describe the growth of density fluctuations in the expanding Universe. The first approach proposed by Zeldovich [1, 2] in 1970 is known as the Zeldovich approximation. The second analytic approach to the formation of the large-scale structure of the Universe [20, 36, 37] is based on the vector BE, which is a natural generalization of the one-dimensional BE [38, 39]. In this approach, the multi-stream flow of gravitationally interacting particles in regions with increased density, which leads to matter localization, is modeled by the ‘viscous’ term in the BE. In the limit of vanishing viscosity, this is equivalent to adhesion of particles, and hence this method is often referred to as the adhesion model (see, e.g., [30, 40–45]).

The limit version of the AM describes the characteristic mosaic structure of matter distribution in the Universe in a natural way. The principal elements of the ‘mosaic’ in three-dimensional space (vertices, edges, faces, and cell volumes) can be associated with the observed structures of the 3D galaxy distribution (compact galaxy clusters, filaments and chains of galaxies, sheets with a relatively high density of galaxies, and empty dark voids between them).

Both numerical simulation of gravitational interaction and the analytic methods mentioned above require the initial conditions to be specified. At the linear stage of the gravitational instability development, density fluctuations are assumed to be random Gaussian fields, which corresponds to the results of the analysis of CMB fluctuations with good accuracy [10]. Statistical properties of such fields are fully determined by the characteristic amplitude and spatial spectral density of fluctuations. In cosmology, it is common to normalize the initial spectrum by the parameter σ_8 (see Table 1), which corresponds to root-mean square density field fluctuations smoothed by a top-hat filter with the radius $8h^{-1}$ Mpc according to the assumption that the evolution is described by the linear theory. Both the amplitude and the spectral density of the initial fluctuations are determined from CMB observations with an accuracy of about a few percent. The amplitude of temperature fluctuations suggests that the characteristic spatial scales of density fluctuations, which presently reach the nonlinear stage, are $\sim 2\text{--}6$ Mpc, depending on the method of estimation. These scales (2–6 Mpc) are in good agreement with observations of the large-scale structure galaxy distribution. The exponents of power-law spectra of the initial (linear) density fluctuations are fully determined by the parameters of the cosmological model. On large scales (for small wave numbers k), the spatial density spectrum behaves as

$$P(k) \propto k^n,$$

where $n \approx 1$ (see Table 1) determines the so-called Zeldovich spectrum. On smaller scales (with larger wave numbers), the spatial spectrum smoothly transforms into the quasi-power-law spectrum

$$P(k) \propto k^{-3} \ln k. \quad (4)$$

The transition of the perturbation spectrum from one limit case to another is fully determined by cosmological parameters and can be calculated, for example, using the well-known code for CMB anisotropy calculations,

CMBFAST [46]. Calculations and observations suggest that presently, near the nonlinearity scale value (formally determined by Eqn (17) below), $P(k) \propto k^{-1.5}$.

In this review, we discuss the evolution of the growing mode of gravitational instability for the dark matter density. Luminous objects in the Universe consist of baryons; therefore, it is also important to take the dynamics of the baryonic component in the Universe into account. The reader can find more on this topic in paper [47], which proposes an interesting generalization of the model described here when the baryon dynamics is taken into account.

3. Equations for the gas of gravitationally interacting particles

The evolution of inhomogeneous matter density fluctuations in the Universe is properly described by three partial differential equations: the continuity equation, the Euler equation, and the Poisson equation (see, e.g., [28–31]). To exclude the homogeneous component of the expanding Universe, the comoving reference frame \mathbf{x} (the one moving with the homogeneous expansion of the Universe) and the corresponding peculiar velocity \mathbf{u}_p are typically used:

$$\mathbf{r} = a(t)\mathbf{x}, \quad \dot{\mathbf{r}} = H(t)\mathbf{r} + \mathbf{u}_p. \quad (5)$$

The monotonically increasing function $a(t)$, which takes the homogeneous expansion of the Universe into account, is usually called the scale factor. If we normalize the scale factor to unity at the present epoch, then $a(t)$ is simply expressed through the redshift z : $a(t) = (1+z)^{-1}$. Correspondingly, the Hubble constant determined by relation (1) is given by

$$H(t) = \frac{d \ln a(t)}{dt}.$$

The scale factor is uniquely determined by the cosmological model parameters. For example, in the Einstein–de Sitter model with $\Lambda = 0$ and $\Omega = 1$, we have $a(t) \propto t^{2/3}$. In the more realistic Λ CDM model, the scale factor is represented by a somewhat more complicated but known function of time [48].

It is known that during the evolution of the Universe, neither peculiar velocities nor the gravitational potential reach relativistic values. For this reason, in studies of the evolution of density perturbations in the Universe, the use of classical mechanics and the Newtonian gravitational potential is well justified. In the reference frame specified above, in terms of peculiar velocities \mathbf{u}_p , the continuity, Euler, and Poisson equations describing the gravitational instability in the expanding Universe take the respective forms

$$\begin{aligned} \frac{\partial \rho}{\partial t} + \frac{1}{a} \nabla(\rho \mathbf{u}_p) &= -3H\rho, \\ \frac{\partial \mathbf{u}_p}{\partial t} + \frac{1}{a} (\mathbf{u}_p \nabla) \mathbf{u}_p &= -\frac{1}{a} \nabla \phi - H\mathbf{u}_p, \\ \frac{1}{a^2} \nabla^2 \phi &= 4\pi G(\rho - \bar{\rho}), \end{aligned} \quad (6)$$

where ρ and $\bar{\rho}$ are the density and the mean density of matter and ϕ is the gravitational potential that appears due to inhomogeneities in the matter distribution.

In Eqns (6), pressure forces are ignored because we are studying the medium consisting of particles that interact only gravitationally. In the first two equations of system (6), the continuity equation and the Euler equation, the terms $-3H\rho$

and $-H\mathbf{u}_p$ in the right-hand sides take the expansion of the Universe into account; the factor $1/a$ appears as a result of differentiation in the comoving frame \mathbf{x} :

$$\nabla \equiv \frac{\partial}{\partial x_i} \equiv a(t) \frac{\partial}{\partial r_i}.$$

System of equations (6) should be solved by specifying the initial density fluctuations and a smooth initial velocity field.

The evolution of density perturbations, as long as their amplitude is small, is described in the linear approximation by equations obtained from linearization of system of equations (6). The exact solution of the linearized equations involves a growing mode, which is the main object of our analysis, and two decaying modes, which can be neglected in the subsequent analysis. The velocity field of the growing mode is a potential vector field proportional to the gradient of the linear gravitational potential:

$$\mathbf{u}_{p, \text{lin}} \propto -\nabla \phi_{\text{lin}}.$$

In the linear mode, the spatial structure of density perturbations (in the comoving frame) remains unchanged, while the amplitude of density perturbations is proportional to the growing mode: $\delta \propto D(t)$ in Eqn (3), determined by the cosmological model parameters [48]. For example, in the Einstein–de Sitter model, $D(t)$ is a monotonically increasing function of time:

$$D(t) \propto a(t) \propto t^{2/3}.$$

Equations (6) describing the evolution of perturbations in the Universe become more convenient for analysis after the following change of variables proposed in [49]:

$$\rho = a^{-3}\eta, \quad \mathbf{u}_p = a\dot{D}\mathbf{v}, \quad \phi = \left(\frac{3}{2}\Omega_0\dot{a}^2D\right)\varphi. \quad (7)$$

In addition, we use the variable D , a monotonically increasing function of time t , instead of time t . As a result, the system of equations takes the forms

$$\begin{aligned} \frac{\partial \eta}{\partial D} + \nabla(\eta\mathbf{v}) &= 0, \\ \frac{\partial v_i}{\partial D} + (\mathbf{v}\nabla)\mathbf{v} &= -\frac{3}{2}\frac{\Omega_0}{Df^2}(\nabla\varphi + \mathbf{v}), \\ \nabla^2\varphi &= \frac{\delta}{D}, \end{aligned} \quad (8)$$

where $\Omega_0 = \bar{\rho}_m/\rho_c$ is the ratio of the mean density at the present time to its critical value $\rho_c = 3H_0^2/8\pi G$, $f = d \ln D / d \ln a$, and $\delta = (\eta - \bar{\eta})/\bar{\eta}$, where $\bar{\eta} = \Omega_0\rho_c = \text{const}$. The meaning of the transition to Eqns (8) is that their left-hand sides have the form of standard hydrodynamic equations. As we see in what follows, the right-hand side of the Euler equation vanishes in both the ZA and AM, and the Poisson equation can be omitted in the linear approximation. Hence, it becomes possible to extend many results obtained in the Burgers hydrodynamic turbulence model to the cosmological problem of the structure formation in the Universe.

The second equation of system (8) can be simplified after introducing the full derivative

$$\frac{d}{dD} \equiv \frac{\partial}{\partial D} + v_k \frac{\partial}{\partial x_k},$$

where summation over repeated indices is understood. Then the second equation of system (8) takes the form

$$\frac{d\mathbf{v}}{dD} = -\frac{3}{2}\frac{\Omega_0}{Df^2}(\nabla\varphi + \mathbf{v}). \quad (9)$$

It is easy to verify that in the linear mode (which is valid if $\sqrt{\langle \delta^2 \rangle} \ll 1$), the growing mode of linearized system (8) takes the form

$$\begin{aligned} \delta(\mathbf{q}, D) &= D \nabla_{\mathbf{q}}^2 \Phi_0(\mathbf{q}), \\ \mathbf{v}(\mathbf{q}, D) &= \mathbf{v}_0(\mathbf{q}) = -\nabla_{\mathbf{q}} \Phi_0(\mathbf{q}), \\ \varphi(\mathbf{q}, D) &= \Phi_0(\mathbf{q}), \end{aligned} \quad (10)$$

where \mathbf{q} are Lagrangian coordinates of a liquid particle and $\Phi_0(\mathbf{q})$ is the initial value of the gravitational potential. Solution (10) describes density, velocity, and gravitational potential perturbations in the Lagrangian space. We stress that in the linear approximation, the gravitational potential and the velocity potential have the same spatial structure, and they simply coincide in the chosen dimensionless variables. To find these fields in the Eulerian space, it is necessary to solve equations for particle trajectories

$$\mathbf{x}(\mathbf{q}, D) = \mathbf{q} + D\mathbf{v}_0(\mathbf{q}), \quad (11)$$

for $\mathbf{q} = \mathbf{q}(\mathbf{x}, D)$ and to substitute the solution in (10). We recall that the initial field of the gravitational potential $\Phi_0(\mathbf{q})$ is determined by the initial density perturbations in the linear mode, which are assumed to be a random Gaussian field. The power-law spectrum (see Fig. 5 in Section 4.2), which uniquely determines the statistical properties of this Gaussian field, can be found from CMB observations (see, e.g., [9]).

Although the velocity \mathbf{v} remains constant for each particle in the linear regime, the physical, peculiar velocity \mathbf{u}_p changes with time [see (7)]. In the growing mode (10), gravitational forces proportional to $\partial\varphi/\partial x_i$ are balanced by resistance forces $H\mathbf{u}_p \propto \mathbf{v}$, which appear in the expanding Universe. Correspondingly, in the linear approximation, the right-hand side of Eqn (9) vanishes, and the equation of motion in the Eulerian representation becomes

$$\frac{d\mathbf{v}}{dD} \equiv \frac{\partial \mathbf{v}}{\partial D} + (\mathbf{v}\nabla)\mathbf{v} = 0. \quad (12)$$

We note that the reduction of the Euler equation to Eqn (12), from which solution (11) follows, had been misunderstood by some cosmologists and many observers for many years. The zero right-hand side of the Euler equation was interpreted as the total disregard of gravity. Therefore, Zeldovich's conclusion about the formation of pancakes at the nonlinear stage was regarded as an unjustified extension of the result valid only in the medium of noninteracting particles to a gravitating medium.

4. The Zeldovich approximation

In 1970, Zeldovich found solutions of the gravitational instability equations at the linear stage of evolution and extended these solutions to the early nonlinear stage of gravitational instability [1, 2] (also see [30]). Such an extension assumes that the initial perturbations are sufficiently smooth in the sense that the initial power spectrum must decay faster than k^{-3} as $k \rightarrow \infty$. In realistic cosmological models, for example in the Λ CDM model, the spectrum

follows the law $P(k) \propto \ln(k)k^{-3}$ up to very large wavenumbers, at which cosmological assumptions become invalid. Therefore, to be applied at formation scales of galaxy clusters and superclusters, the ZA must be modified. Such a modification is discussed in Section 4.2.

4.1 Basic equations

The Zeldovich approximation can be visually interpreted as the map given by relations (11) from the Lagrangian space $L\{\mathbf{q}\}$ to the Eulerian space $E\{\mathbf{x}\}$. The illustration of this map for four stages of the density field evolution is given in Fig. 3. The stages are marked by the value of the parameter $\sigma = \langle \delta_{\text{lin}}^2 \rangle^{1/2}$, where δ_{lin} is the normalized density fluctuations (the so-called density contrast),

$$\delta_{\text{lin}} \equiv \frac{\rho(\mathbf{x}, t) - \bar{\rho}(t)}{\bar{\rho}(t)} = \frac{\eta(\mathbf{x}, D) - \bar{\eta}}{\bar{\eta}}. \quad (13)$$

For convenience, the parameter σ is calculated in the framework of the linear theory, where $\sigma \propto D(t)$.

In two dimensions, the ZA equations for velocity are equivalent to equations for the inclination angle of the wave front and intensity of an optical wave incident on a phase

screen. The variable $D(t)$ then plays the role of the distance from the phase screen. The bright caustic on the floor of a swimming pool with a wavy surface on a sunny day (Fig. 3e) properly reflect the density distribution in the 2D case [50].

Using the mass conservation in the form

$$\eta d^3x = \bar{\eta} d^3q,$$

where \mathbf{q} are the initial particle coordinates, which we call the Lagrangian coordinates, and \mathbf{x} is the comoving reference frame, which we refer to as the Eulerian frame, Zeldovich derived the expression for the current density as a function of $D(t)$ and the Lagrangian coordinate \mathbf{q} :

$$\eta(\mathbf{q}, D) = \frac{\bar{\eta}}{(1 - D\lambda_1(\mathbf{q}))(1 - D\lambda_2(\mathbf{q}))(1 - D\lambda_3(\mathbf{q}))}, \quad (14)$$

where $\lambda_1(\mathbf{q})$, $\lambda_2(\mathbf{q})$, and $\lambda_3(\mathbf{q})$ are eigenvalues of the deformation tensor $d_{ij} = \partial^2 \Phi_0 / \partial q_i \partial q_j$.

The distribution function of eigenvalues of the deformation tensor for Gaussian random fields, which plays a major role in many cosmological issues related to structure formation (see, e.g., [51–53]), was found by Doroshkevich [54]:

$$P(\lambda_1, \lambda_2, \lambda_3) = \frac{675\sqrt{5}}{8\pi\sigma_\delta^6} (\lambda_1 - \lambda_2)(\lambda_1 - \lambda_3)(\lambda_2 - \lambda_3) \times \exp \frac{-6I_1^2 + 15I_2}{2\sigma_\delta^2}. \quad (15)$$

Here and below, we assume that the eigenvalues are ordered,

$$\lambda_1 \geq \lambda_2 \geq \lambda_3,$$

and the exponent depends on invariants of the deformation tensor

$$I_1 = \lambda_1 + \lambda_2 + \lambda_3, \quad I_2 = \lambda_1\lambda_2 + \lambda_1\lambda_3 + \lambda_2\lambda_3. \quad (16)$$

It follows from (15) that the probability of finding two or three equal eigenvalues is zero. Nevertheless, there are points where $\lambda_1 = \lambda_2$ or $\lambda_2 = \lambda_3$, but no points where all three eigenvalues coincide. The set of points with two equal eigenvalues consists of one-dimensional lines, and therefore has measure zero. Correspondingly, the probability of finding two equal eigenvalues is zero. From the standpoint of dynamics, the above statement means that spherical collapse is specifically forbidden, while the collapse into a line is possible, although it is different from the cylindrically symmetric case, even locally [55].

In cosmology, initial conditions are usually characterized by the initial perturbation spectrum $P_\delta(k)$ (see also Fig. 5 in Section 4.2), which is connected with the spectrum of the gravitational potential by the obvious relation $P_\delta = k^4 P_{\Phi_0}$. Similarly to what we did at the linear stage, we can find the density field in the Eulerian representation by solving Eqn (11) for \mathbf{q} and substituting the obtained solution in Eqn (14). For realistic initial conditions, this procedure requires numerical methods.

As follows from relation (14), for smooth initial conditions, density peaks first arise around the largest eigenvalue λ_1 (we recall that we label the eigenvalues for any \mathbf{q} in decreasing order, $\lambda_1 \geq \lambda_2 \geq \lambda_3$). These clumps have an oblate form because the other eigenvalues are smaller than λ_1 . In

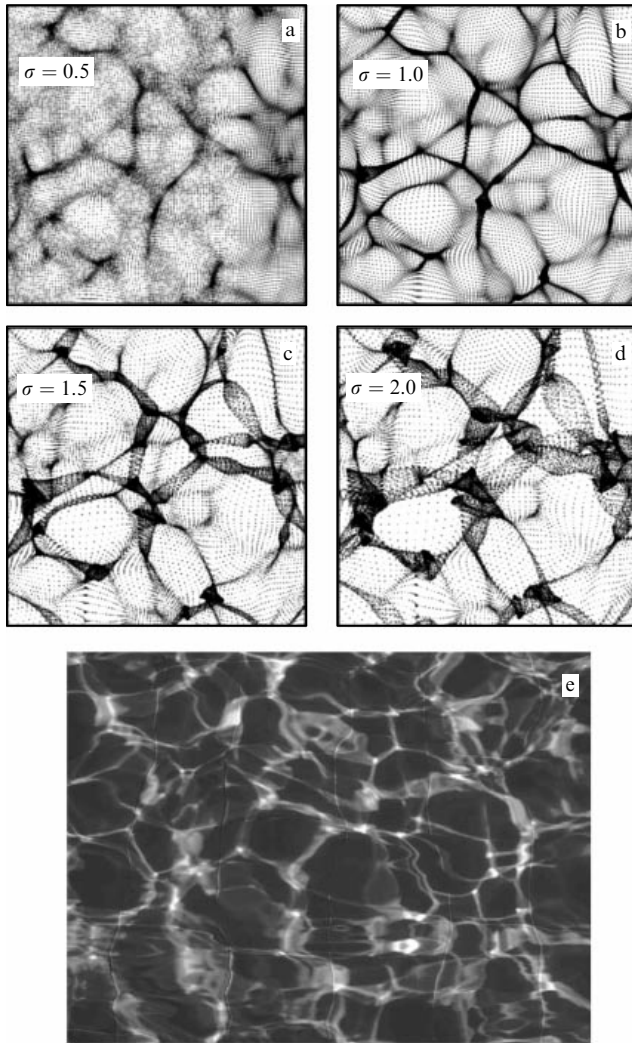


Figure 3. (a–d) The Zeldovich approximation in two dimensions for different values of the parameter $\sigma = \langle \delta_{\text{lin}}^2 \rangle^{1/2}$, where δ_{lin} is given by Eqn (13). (e) Caustic on the floor of a swimming pool.

cosmology, such objects are referred to as ‘Zeldovich pancakes’. Their form is qualitatively different from the density clumps predicted by the linear theory, according to which the clumps first emerge in the vicinity of peaks of the sum $\delta = \lambda_1 + \lambda_2 + \lambda_3$. In fact, the difference in the location of Zeldovich pancakes from that of density clumps predicted by the linear theory is not large because of a significant correlation between δ and the maximum eigenvalue λ_1 : $\langle \lambda_1 \delta \rangle / (\sigma_{\lambda_1} \sigma_\delta) \approx 0.49$.

We note that the results of numerically solving the N -body problem are in good agreement with the ZA predictions [56]. The Zeldovich pancakes emerge in collisionless dark matter as regions with three-stream flows particle motions restricted by caustics—surfaces with formally infinite density. The form and other characteristics of Zeldovich pancakes, as well as other features of the characteristic spatial structure of the density field shown in Fig. 3, are determined by the catastrophe theory [55]. Although the difference between the high-density regions and multi-stream flow regions had not been stressed for many years, it was recently clearly demonstrated in [57, 58].

Later, it was discovered that the ZA correctly describes the behavior of density fluctuations only until caustics emerge, i.e., at the stage corresponding to $\sigma_\delta \lesssim 1$ (see, e.g., review [30] and the references therein). At $\sigma_\delta > 1$, formula (11) predicts a much more rapid broadening of multi-stream flow regions than follows from the N -body simulations [34, 35, 59]. This is clearly seen from a comparison of Figs 3b, d with Fig. 4. From Figs 3b, d and 4, in spite of the difference in the corresponding initial conditions, it is evident that correctly taking gravitational interactions into account leads to the formation of much thinner pancakes than the ZA predicts. This discrepancy between the N -body simulations and the ZA stimulated the development of the AM, which is discussed in Section 5. In Section 4.2, we briefly discuss modifications of the ZA, which allow generalizations to the case where the power-law behavior of the spectrum on small scales cannot be disregarded any more [60, 61].

4.2 The modified Zeldovich approximation

We note that the 2D and 3D N -body results very weakly depend on the initial density perturbations on small scales [62–64]. We stress that a similar effect is observed in the Burgers turbulence [65, 66], in which the behavior of large-scale structures weakly depends on low-scale components. In the case of gravitationally interacting particles, the large-scale structure formation is mostly affected by those initial density perturbations that have currently reached the stage of non-linear gravitational instability [63]. This fact allows using an

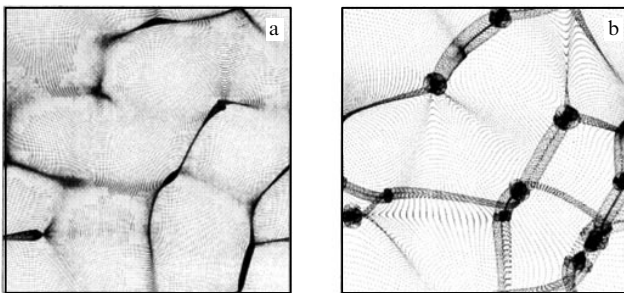


Figure 4. The distribution of gravitationally interacting particles numerically obtained at two stages: (a) $\sigma_\delta = 1$ and (b) $\sigma_\delta = 2$.

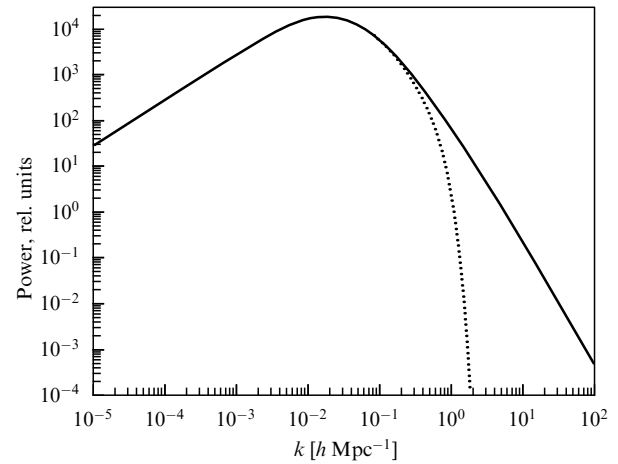


Figure 5. The initial power-law spectrum in the cosmological Λ CDM model (solid curve) and the corresponding initial spectrum with a cut-off at the current nonlinear scale (dashed curve).

auxiliary model leading to a large-scale structure similar to what is formed in the initial model but ignoring tiny small-scale structure details [60, 61]. The intermediate scale that separates the large-scale structure from the small-scale one at a time t corresponds to the nonlinearity scale l_{nl} , which is determined by the solution of the equation

$$\delta_{rms}^2(l_{nl}) \equiv 4\pi D^2 \int_0^\infty P_{lin}(k) W(k, l_{nl}) k^2 dk = 1, \quad (17)$$

where $W(k, l_{nl})$ is the filter function. For example, the initial power-law spectrum in the currently popular Λ CDM model is shown in Fig. 5 by the solid curve, and the corresponding spectrum with a low-scale cut-off is shown by the dashed curve.

If the amplitudes and phases of the initial perturbations in both models are the same, then the auxiliary model with a cut-off power-law spectrum yields a large-scale structure very similar to the one that emerges from the spectrum without a cut-off. The dashed curve in Fig. 5 corresponds to a Gaussian window cut-off. A simpler cut-off, with the spectrum set to zero for $k > k_{nl} \simeq 1/l_{nl}$, where k_{nl} is determined from the equation

$$4\pi D^2 \int_0^{k_{nl}} P_{lin}(k) k^2 dk = 1, \quad (18)$$

yields a similar large-scale structure. The auxiliary model with a cut-off initial spectrum allows using the ZA, which requires smooth initial perturbations and better understanding complex nonlinear processes that affect the large-scale structure formation. The loss of low-scale structure details that are present in the original model with the full spectrum is the price to be paid for such a simplification. The AM described in Section 5 was developed to correct this shortcoming of the ZA.

In conclusion, it is useful to note that both the ZA (Fig. 3b, d) and numerical N -body results (see Fig. 4) give rise to an irregular mosaic large-scale structure of the Universe in which relatively thin pancakes with high galaxy number density enclose ‘dark volumes’ with a low number density of galaxies, corresponding to single-stream regions.

However, the results of direct numerical modeling show that after the appearance of singularities, their width increases much more slowly than follows from the Zeldovich theory [30]. This is because the returning force starts pulling a particle passed through the singularity because of the enhanced density there, such that particles start oscillating in the vicinity of a singularity. To describe the effect of transition from large-scale motions to low-scale oscillations semiquantitatively, the diffusion term $\nu \nabla^2 \mathbf{v}$ was introduced into the equation of motion [20, 36, 37], which must approximately describe a ‘sticking’ of particles near singularities caused by gravity. That is why this model is called the adhesion model in cosmology.

The ZA has been carefully tested by comparing it with the results of numerical calculations [60, 61, 67–69]. These results have been reviewed several times [4, 30, 31], and we do not repeat them here. We note only that in [67] (see also [4, 30]), an analytic estimate of the accuracy of the ZA was obtained, which was subsequently rederived by Mukhanov [9]; however, it was given erroneously in [9]. The estimate is based on the determination of the self-consistency level of the ZA, which can be quantitatively expressed by the ratio of the difference between the density ρ_{ZA} in (14) predicted by the ZA and the density ρ calculated using the Poisson equation, and ρ_{ZA} :

$$\Delta \equiv \frac{\rho - \rho_{ZA}}{\rho_{ZA}} \equiv \frac{\eta - \eta_{ZA}}{\eta_{ZA}} = -D^2 I_2 + 2D^3 I_3,$$

where I_2 is determined by Eqn (16) and $I_3 = \lambda_1 \lambda_2 \lambda_3$. This estimate shows, in particular, that an arbitrary one-dimensional perturbation is described by the ZA exactly until the appearance of multi-stream flow regions and that by the time the singularity is reached ($D = 1$), the density error remains finite.

To conclude this section, we present Fig. 6, which allows comparing the ZA and AM with the results of 3D numerical calculations in the standard cosmological model [70, 71]. This figure shows thin slices of the 3D density distribution obtained in the AM (Fig. 6a), in 3D numerical simulations of the structure evolution (Fig. 6b), and in the ZA (Fig. 6c). Initial conditions in all models were taken to be the same and corresponded to those in the standard cosmological model with the initial spectrum shown in Fig. 5 by the solid curve.

4.3 Lagrangian and Eulerian statistics of matter

We recall that the Zeldovich formation model of the large-scale structure of the Universe at the early nonlinear stage was discussed in Section 4.2. The Zeldovich analysis of model

equations of motion was carried out in the Lagrangian space, whereas the particle distribution in the Eulerian space is of most interest. In addition, although the Zeldovich model uses dynamical equations (e.g., Eqn (11), which connects the Lagrangian and Eulerian coordinates of the particle motion), the fields themselves are initially chaotic due to generic randomness of matter density perturbations in the early Universe.

Therefore, the analysis of matter distribution in the Universe in the framework of the Zeldovich model assumes a statistical analysis of random matter density fields, which is based on relations between statistical characteristics of fields in the Lagrangian and Eulerian representations. Below, we indicate some relations of the Lagrangian and Eulerian statistics and then use them to analyze statistical properties of the large-scale structure of the Universe in the Zeldovich model framework.

We start with the general relation between the Lagrangian and Eulerian coordinates of a hydrodynamic motion of particles $\mathbf{x} = \mathbf{X}(\mathbf{q}, t)$. We note that in the particular case of a vector function $\mathbf{X}(\mathbf{q}, t)$, the last equality passes into Zeldovich relation (11) after the change of variables $D \rightarrow t$:

$$\mathbf{x} = \mathbf{q} + t \mathbf{v}_0(\mathbf{q}), \quad \mathbf{v}_0(\mathbf{q}) = -\nabla_{\mathbf{q}} \Phi_0(\mathbf{q}). \quad (19)$$

We call the field $\mathbf{X}(\mathbf{q}, t)$ the Lagrangian field of Eulerian coordinates of a particle. In addition, we introduce the Lagrangian field of particle density $R(\mathbf{q}, t)$, which, as is well known, has the form

$$R(\mathbf{q}, t) = \frac{\rho_0(\mathbf{q})}{J(\mathbf{q}, t)}, \quad (20)$$

where $\rho_0(\mathbf{q})$ is the initial density field and $J(\mathbf{q}, t)$ is the Jacobian of the transformation from Eulerian to Lagrangian coordinates,

$$J(\mathbf{q}, t) = \left| \frac{\partial \mathbf{X}(\mathbf{q}, t)}{\partial \mathbf{q}} \right|, \quad J(\mathbf{q}, t=0) = 1. \quad (21)$$

Assuming all fields to be random, we introduce the distribution of Lagrangian coordinate and density fields

$$f_L(\mathbf{x}, \rho; \mathbf{q}, t) = \langle \delta(\mathbf{X}(\mathbf{q}, t) - \mathbf{x}) \delta(R(\mathbf{q}, t) - \rho) \rangle. \quad (22)$$

In what follows, we call such distributions Lagrangian distributions, and analogous field distributions in the Eulerian space are called Eulerian distributions. As we show below, distribution (22) is tightly connected with the Lagrangian probability density of coordinate fields, which is more

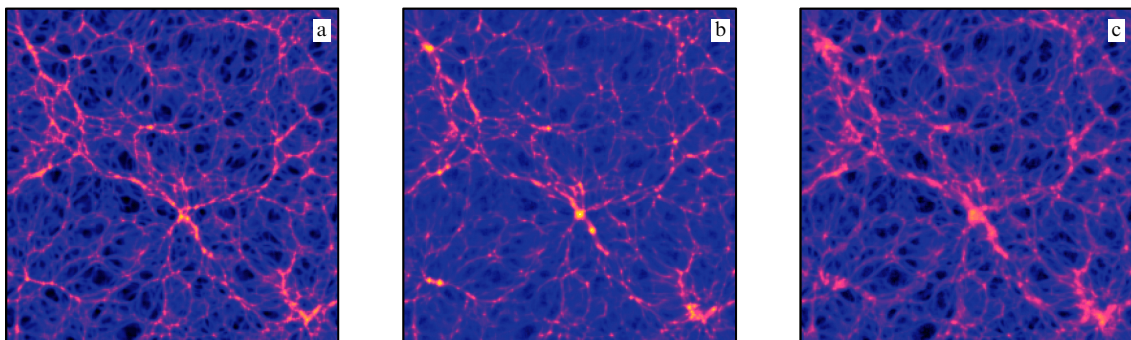


Figure 6. Three thin slices of the 3D density distribution obtained in the standard cosmological model for the same initial conditions: (a) AM, (b) 3D numerical model, and (c) ZA [70, 71].

convenient for manipulations, and the Jacobian:

$$f_L(\mathbf{x}, j; \mathbf{q}, t) = \langle \delta(\mathbf{X}(\mathbf{q}, t) - \mathbf{x}) \delta(J(\mathbf{q}, t) - j) \rangle.$$

We next discuss formulas connecting Lagrangian field distributions with the corresponding Eulerian fields. The Eulerian field of Lagrangian coordinates of particles $\mathbf{q}(\mathbf{x}, t)$ is inverse to the Lagrangian field of Eulerian coordinates $\mathbf{X}(\mathbf{q}, t)$. In addition, the Eulerian density and Jacobian fields are expressed as

$$\rho(\mathbf{x}, t) = R(\mathbf{q}(\mathbf{x}, t), t), \quad j(\mathbf{x}, t) = J(\mathbf{q}(\mathbf{x}, t), t).$$

We first consider the Eulerian probability density

$$f_E(\mathbf{q}, j; \mathbf{x}, t) = \langle \delta(\mathbf{q}(\mathbf{x}, t) - \mathbf{q}) \delta(j(\mathbf{x}, t) - j) \rangle.$$

We temporarily assume that the functions $\mathbf{x} = \mathbf{X}(\mathbf{q}, t)$ and $\mathbf{q} = \mathbf{q}(\mathbf{x}, t)$ are one-to-one maps of the Lagrangian coordinates \mathbf{q} into Eulerian ones, and vice versa. Then the relation that connects the delta-functions of a nonlinear argument holds (see, e.g., [72]):

$$j(\mathbf{x}, t) \delta(\mathbf{X}(\mathbf{q}, t) - \mathbf{x}) = \delta(\mathbf{q}(\mathbf{x}, t) - \mathbf{q}).$$

Using this formula and the ‘puncturing’ property of the delta-function (see [72] for more details, as well as [42]), it is easy to obtain the following formula connecting the Lagrangian and Eulerian distributions:

$$f_E(j; \mathbf{x}, t) = j \int f_L(\mathbf{x}, j; \mathbf{q}, t) d\mathbf{q}. \quad (23)$$

Using Eqns (20) and (23), we can easily obtain a similar relation for more ‘physical’ Eulerian and Lagrangian distributions describing the matter density statistics:

$$\rho f_E(\rho; \mathbf{x}, t) = \int \rho_0(\mathbf{q}) f_L(\mathbf{x}, \rho; \mathbf{q}, t) d\mathbf{q}. \quad (24)$$

More detailed calculations leading to various relations between Eulerian and Lagrangian distributions can be found in [42, 72–74]. Because we are mostly interested in the evolution of the matter density distribution, we present the formula relating the Eulerian and Lagrangian density distributions that follows from (24) in the case of a statistically homogeneous density field with low amplitudes in the early Universe ($\rho \simeq \rho_0 = \text{const}$):

$$f_E^\rho(\rho; t) = \frac{\rho_0}{\rho} f_L^R(\rho; t). \quad (25)$$

The superscript here marks the random variable corresponding to this distribution; for example, $f_L^J(j; t)$ is the Lagrangian distribution of the Jacobian. Taking into account that the density and Jacobian are related by the equation $R = \rho_0/J$, we find

$$f_L^R(\rho; t) = \frac{\rho_0}{\rho^2} f_L^J\left(\frac{\rho_0}{\rho}; t\right).$$

Substituting the last formula in (25), we obtain a very useful formula expressing the Eulerian density distribution through the Lagrangian Jacobian distribution:

$$f_E^\rho(\rho; t) = \frac{\rho_0^2}{\rho^3} f_L^J\left(\frac{\rho_0}{\rho}; t\right). \quad (26)$$

So far, we have discussed relations between Lagrangian and Eulerian random fields assuming the Eulerian density field to be single-stream. However, as noted above, the Zeldovich model of gravitational instability leads to multi-stream flow fields; for example, the Zeldovich pancakes occupy regions of multi-stream flow motion of matter. We therefore present several formulas connecting the Lagrangian and Eulerian statistics that take multi-stream flow motions into account. One such relation has the form

$$\int \rho_0(\mathbf{q}) f_L(\mathbf{x}, \rho; \mathbf{q}, t) d\mathbf{q} = \rho \sum_{N=1}^{\infty} P(N; \mathbf{x}, t) \sum_{n=1}^N f_E^n(\rho; \mathbf{x}, t|N), \quad (27)$$

where $P(N; \mathbf{x}, t)$ is the probability that there are N flows at the moment t at point \mathbf{x} and $f_E^n(\rho; \mathbf{x}, t|N)$ is the Eulerian density distribution of the n th flow, $n = 1, \dots, N$. A similar formula for the Jacobian distribution in the case of a statistically homogeneous matter density field is (see [42])

$$|j| f_L(\mathbf{x}, j, t) = \sum_{N=1}^{\infty} P(N; t) \sum_{n=1}^N f_E^n(j; t|N). \quad (28)$$

Here, the probability $P(N; t)$ bears a clear geometrical meaning: it is equal to the fraction of space volume occupied by N -stream motions.

An important characteristic of the Zeldovich model is the mean number of streams at an arbitrary point in space \mathbf{x} :

$$\langle N(\mathbf{x}, t) \rangle = \sum_{N=1}^{\infty} N P(N; \mathbf{x}, t).$$

In the statistically homogeneous case, it follows from (28) that $\langle N(\mathbf{x}, t) \rangle$ can be expressed through the mean value of the Jacobian modulus:

$$\langle N(\mathbf{x}, t) \rangle = \langle |J(\mathbf{q}, t)| \rangle. \quad (29)$$

We also note that at any point of space except measure-zero regions, the number of streams is odd. Hence, at the early stage, where $\langle N(\mathbf{x}, t) \rangle$ is close to unity, the following approximate equalities are valid:

$$\langle N(\mathbf{x}, t) \rangle \simeq P(1; t) + 3 P(3; t), \quad P(1; t) + P(3; t) \simeq 1. \quad (30)$$

The second expression in (30) is an approximate normalization. Solving Eqns (30) for the relative probabilities, we find

$$P(1; t) \simeq \frac{3 - \langle N \rangle}{2}, \quad P(3; t) \simeq \frac{\langle N \rangle - 1}{2}. \quad (31)$$

These results were used in calculations of the cosmological distribution function of the mass density at the nonlinear stage [75].

4.4 Statistics of flows and matter density distribution

Relations between the Lagrangian and Eulerian distributions presented in Section 4.3 can be used to study some characteristic features of matter density fields in the framework of the Zeldovich model. For simplicity, we consider the two-dimensional model. We note, however, that similar calculations can also be carried out in the three-dimensional case.

We first find the Lagrangian field of the Jacobian of the transformation of Eulerian to Lagrangian coordinates. It

follows from (19) and (21) that this field is equal to the Jacobian

$$J(\mathbf{q}, t) = \left(1 - t \frac{\partial^2 \Phi_0(\mathbf{q})}{\partial q_1^2}\right) \left(1 - t \frac{\partial^2 \Phi_0(\mathbf{q})}{\partial q_2^2}\right) - t^2 \left(\frac{\partial^2 \Phi_0(\mathbf{q})}{\partial q_1 \partial q_2}\right)^2. \quad (32)$$

Below, we consider the initial potential $\Phi_0(\mathbf{q})$ to be a statistically isotropic Gaussian field with the correlation function

$$\langle \Phi_0(\mathbf{q}) \Phi_0(\mathbf{q} + \mathbf{s}) \rangle = A(s), \quad s = |\mathbf{s}| = \sqrt{s_1^2 + s_2^2}.$$

The terms in the Taylor series expansion of this function are

$$\begin{aligned} A(s) &= A - \frac{\mu^2}{2} s^2 + \frac{\nu^2}{8} s^4 + \dots \\ &= A - \frac{\mu^2}{2} (s_1^2 + s_2^2) + \frac{\nu^2}{8} (s_1^4 + 2s_1^2 s_2^2 + s_2^4) + \dots \end{aligned}$$

Based on the known properties of the Gaussian field $\Phi_0(\mathbf{q})$, we can represent it in a more convenient form. We note that the components of the deformation tensor in Jacobian (32) can be substituted by the statistically equivalent values

$$\frac{\partial^2 \Phi_0(\mathbf{q})}{\partial q_1^2} = \sqrt{2}\alpha + \beta, \quad \frac{\partial^2 \Phi_0(\mathbf{q})}{\partial q_2^2} = \sqrt{2}\alpha - \beta, \quad \frac{\partial^2 \Phi_0(\mathbf{q})}{\partial q_1 \partial q_2} = \gamma,$$

where $\{\alpha, \beta, \gamma\}$ are independent Gaussian variables with zero mean and dispersion ν^2 . Then Jacobian (32) takes the form

$$J = (1 - \sqrt{2}\alpha t)^2 - t^2 \delta^2, \quad \delta = \sqrt{\beta^2 + \gamma^2}. \quad (33)$$

Another form of the Jacobian that is geometrically more suggestive can be written in terms of eigenvalues of the deformation tensor

$$J = (1 - \lambda_1 t)(1 - \lambda_2 t),$$

where

$$\lambda_1 = \sqrt{2}\alpha + \delta, \quad \lambda_2 = \sqrt{2}\alpha - \delta. \quad (34)$$

Clearly, the joint distribution $g(a, d)$ of independent random variables α and δ has the form

$$g(a, d) = \frac{d}{\sqrt{2\pi} \nu^3} \exp\left(-\frac{a^2 + d^2}{2\nu^2}\right), \quad (35)$$

where a and d are the arguments of the joint distribution of the respective random variables α and δ . Correspondingly, the distribution of eigenvalues (34) is expressed as

$$P(\lambda_1, \lambda_2) = \frac{\lambda_1 - \lambda_2}{8\sqrt{\pi} \nu^3} \exp\left(-\frac{3(\lambda_1^2 + \lambda_2^2) - 2\lambda_1 \lambda_2}{16\nu^2}\right). \quad (36)$$

Similarly to distribution (15) of eigenvalues of the deformation tensor, distribution (36) forbids the coincidence of eigenvalues. In other words, cylindrical collapse is forbidden, but the collapse into lines — two-dimensional analogs of Zeldovich pancakes — is possible.

Using formula (33) for the Jacobian and distribution (35), it is not difficult to find the Lagrangian distribution of the

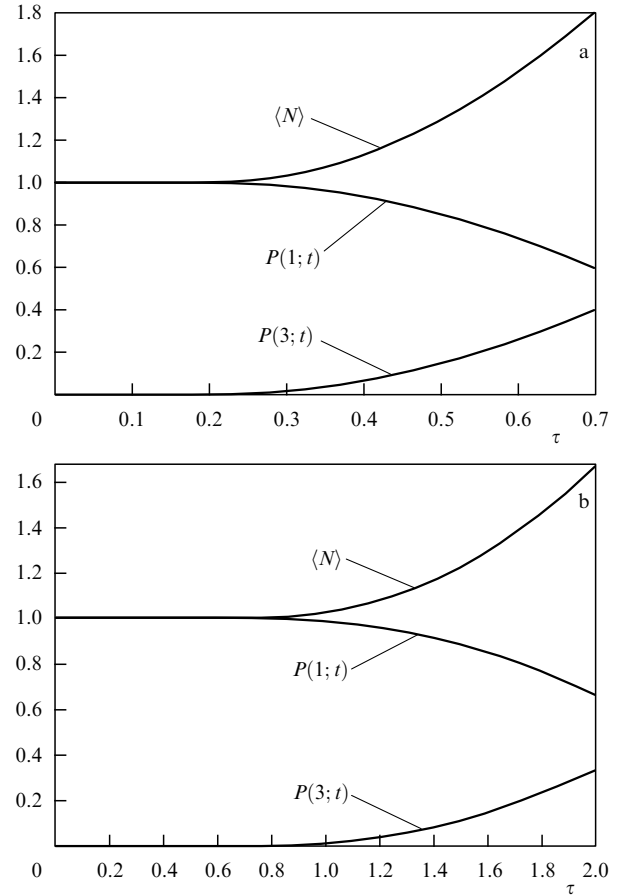


Figure 7. The mean number of flows $\langle N \rangle$ (38) and probabilities of one and three flows as a function of (a) the dimensionless time $\tau = \nu t$ in the 2D Zeldovich model and (b) the parameter $\tau = \sigma_\delta D(t)$ in the 3D version of the Zeldovich approximation.

Jacobian:

$$\begin{aligned} f_L^J(j; t) &= \frac{1}{4\sqrt{3}\tau^2} \exp\left(\frac{3j-1}{6\tau^2}\right) \\ &\times \begin{cases} 2, & j < 0, \\ \operatorname{erfc}\left(\frac{3\sqrt{j-1}}{2\sqrt{3}\tau}\right) + \operatorname{erfc}\left(\frac{3\sqrt{j+1}}{2\sqrt{3}\tau}\right), & j > 0. \end{cases} \quad (37) \end{aligned}$$

Here, the dimensionless time $\tau = \nu t$ is introduced. In turn, the distribution of the Jacobian allows calculating the mean number of matter streams (29):

$$\langle N \rangle = 1 + \frac{4\tau^2}{\sqrt{3}} \exp\left(-\frac{1}{6\tau^2}\right). \quad (38)$$

The τ dependences of the mean number of streams, as well as approximate values (31) of the probabilities $P(1; t)$ and $P(3; t)$ characterizing the region of (two-dimensional) space occupied by one-stream and three-stream flows of matter are shown in Fig. 7a. In Fig. 7b, we present the same curves for the 3D Zeldovich model obtained by numerical integration using Doroshkevich distribution (15) of eigenvalues of the deformation tensor.

After substituting the Lagrangian distribution of Jacobian (37) in a multi-stream-flow analog of relation (26), we obtain the Eulerian distribution of matter density. The presence of a power-law tail (Fig. 8) is the characteristic

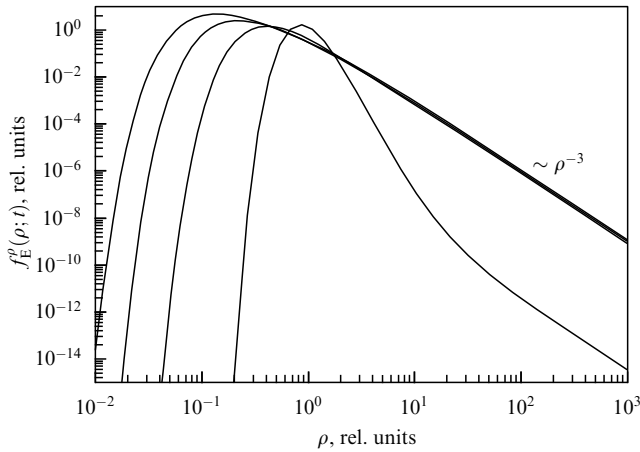


Figure 8. The density distribution in the 2D Zeldovich model for $\tau = 0.1, 0.3, 0.5$, and 0.7 . The power-law tail of the distribution $f_E^{\rho} \propto \rho^{-3}$ is clearly seen.

feature of this distribution:

$$f_E^{\rho}(\rho; t) \simeq C(t) \rho^{-3}, \quad \rho \gg \rho_0, \quad (39)$$

where

$$C(t) = \frac{\rho_0^2}{\sqrt{3} \tau^2} \exp\left(-\frac{1}{6\tau^2}\right).$$

We note that power law (39) provides more evidence of predominantly one-dimensional focusing of matter (see, e.g., [42]) and the formation of Zeldovich pancakes, which are clearly seen in Figs 3 and 4.

4.5 Spectrum of density fluctuations

As noted in Sections 4.1 and 4.2, a relatively fast power-law decrease in the initial density spectrum (4) or even of the cut-off exponential law of the initial spectrum decay shown in Fig. 5 is transformed by the gravitational instability into a spectrum with a heavy power-law tail at large wave numbers. Below, we demonstrate this important fact using the Zeldovich model, which is reduced to Eqns (19).

We consider statistically isotropic density fluctuations, with the correlation function of the density fluctuations

$$B(s, t) = \langle \delta\rho(\mathbf{x}, t) \delta\rho(\mathbf{x} + \mathbf{s}, t) \rangle$$

depending only on the modulus of the vector \mathbf{s} connecting points of observations. It can be shown (see [42]) that in the hydrodynamic approximation, the density correlation function $B(\mathbf{s}, t)$ is expressed through the initial correlation function $B_0(\mathbf{s})$ as

$$B(\mathbf{s}, t) = \int B_0(\mathbf{s}_0) f_L(\mathbf{s}; \mathbf{s}_0, t) d\mathbf{s}_0, \quad (40)$$

where $f_L(\mathbf{s}; \mathbf{s}_0, t)$ is the Lagrangian distribution of the vector of relative particle displacements,

$$f_L(\mathbf{s}; \mathbf{s}_0, t) = \langle \delta(\mathbf{s} - \mathbf{s}_0 + t \nabla_{\mathbf{q}} \psi(\mathbf{q}, \mathbf{s}_0)) \rangle. \quad (41)$$

Here, $\psi(\mathbf{q}, \mathbf{s}_0) = \Phi_0(\mathbf{q} + \mathbf{s}_0) - \Phi_0(\mathbf{q})$.

Before studying the spatial density spectrum corresponding to correlation function (40), we recall that there are several

types of spatial spectra. The first is the one-dimensional spectrum $P(k, t)$ reflecting the spectral properties of density fluctuations $\delta\rho(\mathbf{x}, t)$ as a function of one argument, the coordinate along some direction (for example, the x axis of a Cartesian coordinate system). The correlation function and the one-dimensional spectrum are then related as

$$P(k, t) = \frac{1}{\pi} \int_0^\infty B(s, t) \cos(ks) ds. \quad (42)$$

In the case of anisotropic random fields, the three-dimensional spectrum

$$G(\mathbf{k}; t) = \left(\frac{1}{2\pi}\right)^3 \iiint B(\mathbf{s}, t) \exp(-i\mathbf{k}\mathbf{s}) d\mathbf{s} \quad (43)$$

is frequently considered. If the density field is isotropic, Eqn (43) reduces to

$$G(k, t) = \frac{1}{2\pi^2 k} \int_0^\infty B(s, t) \sin(ks) ds. \quad (44)$$

By comparing Eqns (42) and (44), we find the relation between one-dimensional and three-dimensional spectra:

$$G(k, t) = -\frac{1}{2\pi k} \frac{dP(k, t)}{dk} \Leftrightarrow P(k, t) = 2\pi \int_k^\infty G(k', t) k' dk'. \quad (45)$$

We first calculate the three-dimensional density fluctuation spectrum. Substituting $B(\mathbf{s}, t)$ from (40) in (43), taking (41) into account, and using the ‘puncturing’ property of the delta-function, we obtain

$$G(\mathbf{k}; t) = \left(\frac{1}{2\pi}\right)^3 \iiint B_0(\mathbf{s}_0) \exp(-i\mathbf{k}\mathbf{s}_0) \times \exp\left(-\frac{t^2}{2} \left\langle \left(\mathbf{k} \nabla_{\mathbf{q}} [\Phi_0(\mathbf{q} + \mathbf{s}) - \Phi_0(\mathbf{q})] \right)^2 \right\rangle\right) d\mathbf{s}_0. \quad (46)$$

Here, we used that the initial gravitational potential $\Phi_0(\mathbf{q})$ is Gaussian.

If $\Phi_0(\mathbf{q})$ is an isotropic random field, simple transformations lead to

$$\left\langle \left(\mathbf{k} \nabla_{\mathbf{q}} [\Phi_0(\mathbf{q} + \mathbf{s}) - \Phi_0(\mathbf{q})] \right)^2 \right\rangle = 2k^2 C(s) + 2(\mathbf{s}\mathbf{k})^2 E(s), \quad (47)$$

where

$$C(s) = \frac{1}{s} \frac{dA(s)}{ds} - \frac{1}{s} \frac{dA(s)}{ds} \Big|_{s=0}, \quad E(s) = \frac{1}{s} \frac{dC(s)}{ds}. \quad (48)$$

Substituting (47) and (48) in (46), passing to polar coordinates in the integrand, and performing integrals over angular variables, we obtain

$$G(k; t) = \left(\frac{1}{2\pi}\right)^2 \int_0^\infty B_0(r) \exp(-t^2 k^2 C(r)) \psi(k, r, t) r^2 dr, \quad (49)$$

where

$$\psi(k, r, t) = \sqrt{\frac{\pi}{E(r) t^2 k^2 r^2}} \exp\left(-\frac{1}{4E(r) t^2}\right) \times \operatorname{Re} \left[\operatorname{erf} \left(\frac{i + 2k r t^2 E(r)}{2\sqrt{E(r) t^2}} \right) \right]. \quad (50)$$

We find the asymptotic form of three-dimensional spectrum (50) as $v \rightarrow \infty$. We note that, as follows from the structure of the right-hand sides of (49) and (50), for $k \rightarrow \infty$, $B_0(r)$, $C(r)$, and $E(r)$ can be substituted by their asymptotic expressions as $r \rightarrow 0$:

$$B_0(0) = \sigma^2, \quad C(r) \simeq \frac{v^2}{4} r^2, \quad E(0) = \frac{v^2}{2}.$$

As a result, we obtain

$$G(k, t) \simeq \sigma^2 \left(\frac{1}{2\pi} \right)^{3/2} \exp \left(-\frac{1}{2} v^2 t^2 \right) \times \frac{1}{k} \int_0^\infty \exp \left(-\frac{1}{4} t^2 k^2 v^2 r^2 \right) r dr, \quad k \rightarrow \infty.$$

Integrating, we finally arrive at

$$G(k, t) \simeq \frac{\sigma^2}{v^2} \left(\frac{1}{2\pi} \right)^{3/2} \exp \left(-\frac{1}{2} v^2 t^2 \right) \frac{1}{(kt)^3} \sim k^{-3}, \quad k \rightarrow \infty.$$

After substituting this asymptotic expression in the second expression in (45), we determine the asymptotic form of the one-dimensional spectrum in the Zeldovich model:

$$P(k, t) \sim k^{-1}, \quad k \rightarrow \infty.$$

It can be shown that this asymptotic form is determined by the characteristic behavior of density at the boundaries of volumes that form the Zeldovich pancakes.

5. The adhesion model

The main idea of the AM is to use the ZA determined by Eqns (10) and (11) everywhere except in multi-stream flow regions. This turns out to be possible after introducing a diffusion (viscous) term into the Euler equation in order to prevent particle trajectories from intersecting, and thus make the appearance of multi-stream flow motions impossible. An advantage of such a modified Euler equation is that it strongly slows down the growth in the width of the pancakes and thus neutralizes the main shortcoming of the ZA, although this is achieved by a significant modification of particle trajectories inside the pancakes. Another advantage of the BE is that the smallness of the viscosity coefficient warrants an almost full agreement of the AM with the ZA as long as trajectories do not intersect.

5.1 From the Zeldovich model to the adhesion model

We sketch the derivation of the main equation of the AM. Because the growing mode of gravitational instability is potential at the linear stage, it is natural to introduce the velocity potential Φ related to the particle velocity as

$$\mathbf{v} = -\nabla\Phi.$$

Taking into account that in the linear mode, the velocity potential is approximately equal to the gravitational potential, $\varphi \simeq \Phi$, and adding the viscous term $v\nabla^2\mathbf{v}$ to the right-hand side of the second equation in (8), we arrive at the nonlinear diffusion equation [20, 37]

$$\frac{\partial \mathbf{v}}{\partial D} + (\mathbf{v}\nabla)\mathbf{v} = v\nabla^2\mathbf{v}, \quad (51)$$

which is also referred to as the multidimensional (three-dimensional) Burgers equation. We note an interesting attempt to explain the value of the viscosity coefficient from the dynamics of particle motion in multi-stream flow regions undertaken in [76].

Unlike the Navier–Stokes equation, the BE does not include density. Therefore, this equation does not respect the momentum conservation in general. Only for one-dimensional perturbations and a constant initial density does the BE with vanishing viscosity describe the gas of coalescing particles satisfying the momentum conservation. The location of density clumps (heavy particles) resulting from the merging of light particles coincides with velocity discontinuities in the AM. The coordinates of density clumps formed by the already coalesced particles in the case of an inhomogeneous initial density are different from the location of velocity discontinuities of the BE [77]. In the multidimensional BE, the formation of dense features does not depend on the density behavior, and the density and velocity fields do not satisfy the momentum conservation law even for a constant initial density distribution. This last point is related to the fact that the coalescence of particles with nonplanar geometry, from the standpoint of momentum conservation, corresponds to a medium with variable density. Moreover, in the spherically symmetric case, with the coordinates of the coalesced particles defined formally in accordance with the BE, it follows that the energy of the system increases in the three-dimensional case due to the merging of particles [78].

The relatively good agreement between the motion of gravitationally interacting particles and the solutions of the multidimensional BE is a very nontrivial fact, which apparently can be explained by the random character of initial perturbations. Indeed, the Zeldovich model can be exact only for the growing mode and one-dimensional perturbations. The location of clumps formed by coalesced particles can also be correctly predicted by the BE for one-dimensional perturbations only. Precisely such one-dimensional perturbations are predominantly realized for random initial conditions.

Generally speaking, the term describing the viscosity of the medium can have a different form than the term in Eqn (51) [79]; however, the choice in Eqn (51) reduces the Euler equation in a pressureless medium to the BE, which has an analytic solution. As in the one-dimensional case, the multidimensional BE can be reduced to a linear diffusion equation by the Hopf–Cole substitution [80, 81].

5.2 Calculation of density in the adhesion model, finite viscosity

In cosmology, the AM has been used in two forms. In one of these, the viscosity coefficient v is assumed to be tiny but nonzero, and in the other, it is taken to be infinitely small ($v \rightarrow 0_+$). If the viscosity coefficient is nonzero, then particle trajectories can be found by numerical integration of the equations of motion:

$$\frac{d\mathbf{x}(\mathbf{q}, D)}{dD} = \mathbf{v}(\mathbf{x}(\mathbf{q}, D), D), \quad \mathbf{x}(\mathbf{q}, D=0) = \mathbf{q}. \quad (52)$$

After that, the density of particles can be calculated from the continuity equation [40–42, 59, 69]. An example of the large-scale structure obtained in this way is presented in Fig. 9, which shows the result of numerical modeling of the galaxy

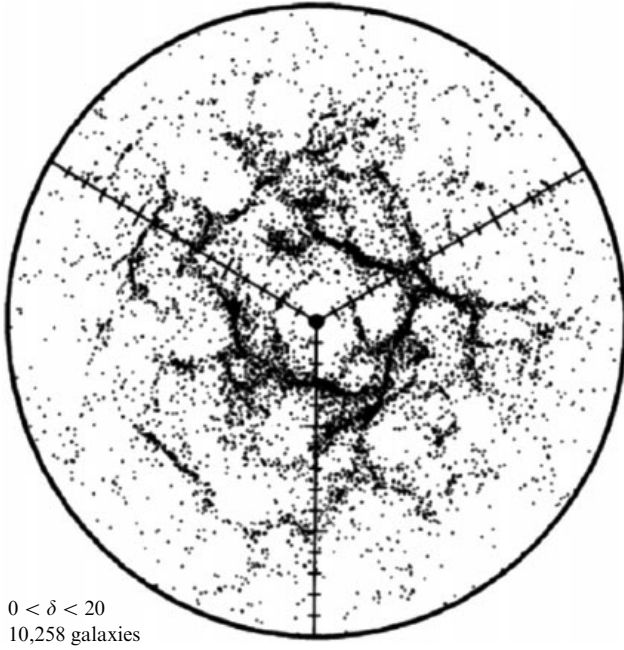


Figure 9. Model distribution of galaxies in the redshift space obtained with the AM in the case of a small but nonzero viscosity coefficient ν [40].

distribution in a thin slice of a three-dimensional volume [40]. We note that Fig. 9 is qualitatively similar to Fig. 1 obtained from the observed galaxy redshift catalog.

In [82], the matter density in one-dimensional Zeldovich pancakes was calculated analytically. It was shown that the fine structure of the matter distribution is different from that predicted by the AM with finite viscosity. To study the dynamics, a discrete matter distribution model—the so-called Q-model [83, 84]—was used; the full description of the numerical scheme can be found in [85].

It was assumed that within a certain interval L on the x axis, all matter is concentrated in N planes, which can be conveniently called particles. The particle density then has the form

$$\rho(x_i, t) = \sum_{x_j} m_j \delta(x_i - x_j), \quad (53)$$

where x_i is the coordinate of the i th particle along the direction of the density and the particle velocity variation. The transition to the continuous model can be done by increasing the number of particles and decreasing the distance between them.

The equation of motion of any particle has the form [85]

$$\frac{d^2 x_i}{dt^2} + 2 \frac{\dot{a}}{a} \frac{dx_i}{dt} - 4\pi G \rho_b(t) x_i = a^{-3} E_{\text{grav}}(x_i, t), \quad (54)$$

where $\rho_b(t)$ is the mean mass density at the time t ,

$$E_{\text{grav}}(x_i, t) = -2\pi G \sum_j m_j \text{sign}(x_i - x_j). \quad (55)$$

We note that the effect of the expansion of the Universe changes the particle dynamics and leads to the appearance of friction-like terms in the equation of motion. In the Einstein–de Sitter model, we can substitute the time $\tau = t_0 \log(t/t_0)$,

and then Eqn (54) takes the form (the Q-model)

$$\frac{d^2 x_i}{d\tau^2} + \frac{1}{3t_0} \frac{dx_i}{d\tau} - \frac{2}{3t_0^2} x_i = E_{\text{grav}}(x_i, \tau), \quad (56)$$

where $t_0^{-2} = 6\pi G \rho(t_0)$. In classical stationary self-gravitating one-dimensional systems, E_{grav} is an invariant of the Lagrange function, proportional to the mass difference on the right and on the left of a given particle at a given time. Therefore, in the time interval between the tangency instants (self-crossing of particle trajectories in the multidimensional case), Eqn (56) has the exact solution [85]

$$X_i(\tau) = c_1^i \exp\left[\frac{2(\tau - \tau^{(n)})}{3t_0}\right] + c_2^i \exp\left(-\frac{\tau - \tau^{(n)}}{t_0}\right) + K_i^n, \quad (57)$$

where $K_i^n = -(3t_0^2/2)E_{\text{grav}}(x_i, \tau)$ is constant between the tangencies. The coefficients c_1^i and c_2^i are determined by the coordinates and velocity of particles at the time of the last tangency. The first and the second terms in (57) respectively correspond to the growing and decaying modes. To find the instant when the coordinates of two adjacent particles coincide, it is necessary to solve a quintic equation; hence, the name of this description, the Q-model.

If all particles have equal masses $m_j = L\rho_0/N$ within the interval L , then the gravity force in (56) becomes $E_{\text{grav}}(x_i, \tau) = N_i L / 3N t_0^2$, where $N_i = N_{i, \text{right}} - N_{i, \text{left}}$ is the difference between the number of particles to the right and to the left of a given particle.

We discuss how the ZA and AM can be obtained from the Q-model. In the ZA, the decaying mode is neglected, i.e., c_2^i in (57) is set to zero. The evolution of the initial perturbation (particle location) in this case is described as

$$X_i(\tau) = \frac{3}{2} w_i^0 t_0 \exp\left(\frac{2\tau}{3t_0}\right) + K_i^n, \quad (58)$$

where w_i^0 is the initial velocity of the i th particle. The substitution of time $D = (3/2)t_0 \exp(2\tau/3t_0)$ reduces solution (58) to an expression describing free particle motion:

$$X_i(D) = w_i^0 D + X_i(0). \quad (59)$$

We recall that in the Zeldovich model, similar relations are assumed to be valid at all times, even when particle self-crossing occurs and the motion becomes multi-stream. On the contrary, in the AM, particles coalesce at the tangency instant, thus forming more massive particles with the mass equal to the sum of masses of the colliding particles and with the velocity determined by momentum conservation. In this model, the decaying mode is also disregarded, i.e., $c_2^i = 0$, both before and after the coalescence of particles.

The evolution in the real dynamical system, i.e., the Q-model, is somewhat intermediate between the evolution of the two models above. However, there are specific conditions under which all three models are equivalent. We take the initial conditions where all coefficients c^i in (57) are zero. Then the initial velocities and densities are correlated such that only the linearly growing mode is excited and expression (57) becomes an exact solution in all three models up to the first collision of particles.

Before describing the evolution of a continuous cluster, we discuss the behavior of two particles with the same mass m located on a segment of length L . In this simple example, we

compare the behavior of particles interacting in the framework of the Q-model and particles in the ZA and the AM with infinitesimal and finite viscosities. We assume that all particles have the mass $m = 1/2$ and that $L = 1$, and introduce dimensionless variables $\theta = \tau/t_0$, $Q_i(\theta) = x_i/L$, and $\beta_i(\theta) = 6\dot{x}_i/t_0L$. Until the first collision of particles, Eqn (57) has the form

$$Q_i(\theta) = c_1^i \exp\left(\frac{2\theta}{3}\right) + c_2^i \exp(-\theta) \mp \frac{1}{4}. \quad (60)$$

We consider a special case of initial conditions where the initial particle velocities and coordinates are chosen such that the coefficients c_2^i are zero in (60). The initial particle velocities are $w_1^0 = -w_2^0 > 0$ and the particles are located symmetrically with respect to the origin. In this case, only the growing mode is excited, and the ZA is an exact solution until particle trajectory crossing occurs. Therefore, it is possible to exactly solve the equations of motion of each particle up to the instant of the first tangency of particle trajectories. The time of the first tangency θ_{cross} is found from Eqn (60): $\theta_{\text{cross}} = -(3/2) \ln \beta(0)$. The particle velocity at this instant is $\beta_{\text{cross},0} = \beta(\theta_{\text{cross}}) = 1$. We note that the time θ_{cross} depends on the initial particle velocity. After the tangency of particle trajectories, the initial balance established between coordinates and velocities is violated, and the condition $c_2^i = 0$ is no longer valid. Therefore, when analyzing Eqn (60) starting from the instant of tangency of trajectories, both the growing and the decaying modes must be taken into account.

After that, particle trajectories start diverging, and their velocities start decreasing because of the gravitational interaction. At $\theta = \theta_{\text{turn}}$, the distance between the particles is maximal, and their velocities are zero, $\dot{q}(\theta_{\text{turn}}) = 0$. For θ_{turn} , we have $\theta_{\text{turn}} = \theta_{\text{cross}} + \bar{\theta}$, $\bar{\theta} = (3/5) \ln 6$. The turn of the particle occurs before it reaches its original position ($|q_i(0)| = (1 - \beta(0))/4$). The corresponding amplitude of the maximum distance $Q_{\text{max},0} = q(\theta_{\text{turn}})$ is

$$Q_{\text{max},0} = \frac{1}{4} - \frac{1}{5} 6^{-3/5} - \frac{1}{20} 6^{2/5} = \alpha \simeq 0.08$$

and is independent of the initial velocity. The decrease in this amplitude occurs due to the presence of a specific friction in Eqn (56) caused by the expansion of the Universe. It is easy to see that the system thus tends to an equilibrium: the localization of particles at the immobile center of mass. The velocity of particles behaves similarly at the instant of the first coincidence of particle locations, also decreasing and becoming equal to $\beta_{\text{ret}} = \beta_{\text{cross},1} = -0.83$.

Thus, it is evident that decaying oscillations of particles occur over large time intervals: particles oscillate with respect to each other with decreasing oscillation amplitude and time between crossings. The dynamics of the oscillations is reduced to a simple iteration scheme [82]. After replacing finite differences by differentials, we obtain

$$\beta_{\text{cross}}(\theta) = \beta_{\text{cross},0} \exp\left[-\frac{1}{9}(\theta - \theta_{\text{cross}})\right], \quad \beta_{\text{cross},0} = 1, \quad (61)$$

$$\Delta q_{\text{max}}(\theta) = 2q_{\text{max},0} \exp\left[-\frac{2}{9}(\theta - \theta_{\text{turn}})\right], \quad q_{\text{max},0} = \alpha, \quad (62)$$

where $\beta_{\text{cross}}(\theta)$ is the dimensionless velocity of particles at the tangency instant and $\Delta q_{\text{max}}(\theta)$ is the maximum distance between particles at time θ .

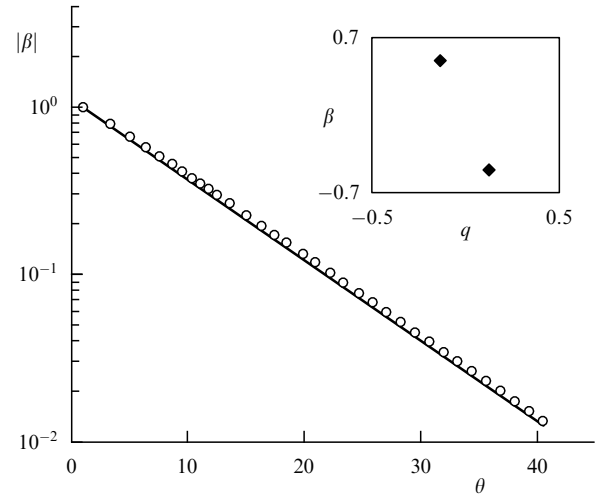


Figure 10. The modulus of the particle velocity β_{cross} as a function of time θ in the linear-logarithmic scale (open circles). The solid curve shows analytic formula (61). Initial conditions are shown in the inset.

Therefore, the velocity of the particles, the distance between them, and the time between tangency instants, $\theta_n(\theta) \sim |\beta_{\text{cross}}(\theta)|$, decay exponentially as functions of the time θ . In terms of the cosmological time t or the new time variable D , the decrease occurs as a power-law function of time, $\beta_{\text{cross}}(t) \sim t^{-1/9} \sim D^{-1/6}$ and $\Delta q_{\text{max}}(t) \sim t^{-2/9} \sim D^{-1/3}$.

Figure 10 presents a comparison of the results of direct numerical simulation and analytic calculations. Shown is the dependence of the modulus of particle velocity β_{cross} on time θ . The solid curve corresponds to calculations using analytic formula (61). The initial conditions are presented in the inset; here, $c_2 = 0$; before the first tangency instant, only the growing mode is therefore taken into account.

We now consider consequences of the analytic models. In the ZA, the law of particle motion does not change after a self-crossing of a trajectory occurs, and the distance between particles increases proportionally to D . In the adhesion approximation with a vanishing viscosity, colliding particles coalesce to form an immobile particle with the mass equal to the sum of the masses of the colliding particles. To describe the motion of particles in the AM with a finite viscosity, we consider the stationary solution of one-dimensional BE (51):

$$V(x, D) = v_{\text{st}}(x) = -U \tanh \frac{x}{\delta}, \quad (63)$$

where $\delta = U/2v$ is the width of the front discontinuity. This solution is also an asymptotic solution of the BE for the step-like velocity profile considered above. The trajectories of individual particles $x(t)$ satisfy Eqn (52), and we have the following expression for particle coordinates:

$$x(D, q) = \delta \operatorname{arsinh} \left[\sinh \left(\frac{q}{\delta} \right) \exp \left(-\frac{UD}{\delta} \right) \right], \quad (64)$$

where q is the Lagrange coordinate. Solution (64) implies that after the particle ‘enters the cluster’ ($x(D, q) \ll \delta$), its coordinate decreases much faster ($x(D, q) \sim \exp[(q - UD)/\delta]$) than in the Q-model.

Paper [82] compares the density profile evolution in the Zeldovich model, Q-model, and AM in the case of the step-

like initial velocity distribution

$$\beta(q) = -\beta_0 \operatorname{sign}(q), \quad (65)$$

where β_0 is a constant coefficient.

In the ZA, particles with an initially negative (as well as positive) coordinate move toward a clump keeping the distance between them unchanged. Hence, until the last particle joins the clump, a two-stream flow occupying the bounded region $2q_{w,\text{Zeld}}$ exists, where $q_{w,\text{Zeld}} = \beta_0 \exp(2\theta/3)/4 = \beta_0 D$ is the clump width in the ZA. We note that the density in each stream is equal to the initial value ρ_0 , i.e., the density is $2\rho_0$ inside the clump ($|q| < q_{w,\text{Zeld}}$).

In the real dynamics, a multi-stream flow process occurs inside the clump, and hence the density at the point with the coordinate q can be obtained by summing the contributions of all flows. Passing in the Q-dynamics to the continuous limit, we can find a closed expression for the mean density of matter in the cluster:

$$\rho(q, \theta) \Big|_{|q| < q_w} = \rho_0 \frac{3}{2q_p} \left[\left(\frac{q_p}{q} \right)^{1/4} - \left(\frac{1}{2\gamma_{\max}} \right)^{1/3} \right], \quad (66)$$

where γ_{\max} is the solution of the equation

$$\gamma_{\max} = \frac{\beta(\gamma_{\max})}{4} \exp\left(\frac{2}{3}\theta\right), \quad (67)$$

and $q_p(\theta)$ is the smallest spatial scale of the internal structure of the clump,

$$q_p = \frac{\chi}{2^{4/3}\beta_0^{1/3}} \exp\left(-\frac{2}{9}\theta\right). \quad (68)$$

The spatial distribution of density inside the clump is characterized by two scales: the characteristic size of the internal structure $q_p(\theta)$, which decays exponentially, $q_p \sim \exp(-2\theta/9)$, and the cluster width q_w , which at the early stage of cluster formation decreases more slowly than the Zeldovich model predicts. The cluster mass also increases with time, in accordance with the AM.

At the final stage of the evolution of an isolated cluster, when all particles reach its inner region, the mass distribution (the mass function) $M(q, \theta)$ has a self-similar form:

$$M(q, \theta) = \int_0^q \rho(\xi, \theta) d\xi = \bar{M}\left(\frac{q}{q_p(\theta)}\right). \quad (69)$$

Therefore, at this evolutionary stage, both the density and the mass function are characterized only by the inner scale of the clump $q_w = q_p(\theta)$. The function $\bar{M}(q/q_p(\theta))$ in the segment $x = [0, 1]$ can be represented in the simple form

$$\bar{M}(x) = 2x^{3/4} - \frac{3}{2}x, \quad (70)$$

where $\bar{M}(1)$ is equal to $1/2$. Expression (70) implies that most of the matter is concentrated in the clump center. For example, half of the total mass (i.e., $2\bar{M}(x_{0.5}) = 1/2$) occupies the interval that is equal to only $x_{0.5} = 0.14$, and 90% of all the mass is distributed over a segment that only slightly exceeds half of the total diameter of the cluster ($x_{0.9} = 0.54$).

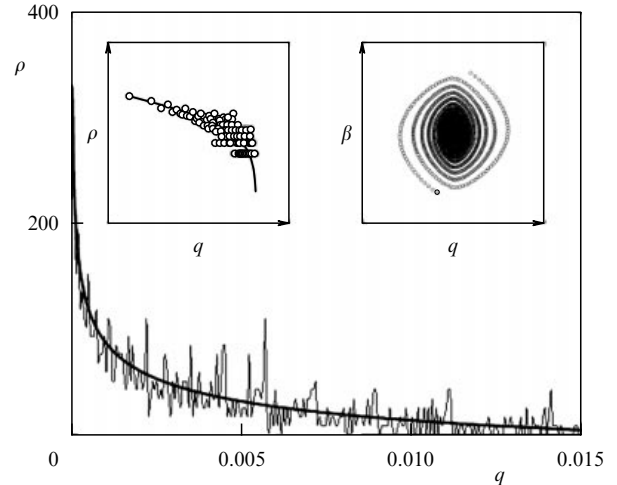


Figure 11. The normalized density ρ as a function of the coordinate q at the late stage for a step-like velocity distribution. The thin and thick curves respectively show the results of modeling and the theoretical dependence. In the left-hand inset, presented is the normalized density ρ as a function of q in the linear–logarithmic scale. White circles correspond to numerical modeling results. The phase plane for $\theta = 23.27$ is shown in the right-hand inset.

Results of the direct numerical simulation [82] of the late evolution of the initial perturbation specified by (65) are in fair agreement with analytic calculations. Figure 11 presents the normalized density profile at the final stage of the evolution (the thin curve) and the theoretical prediction (the thick curve). The same plots are shown in the logarithmic scale in the inset in the left panel of Fig. 11: here, white circles show the results of numerical simulation. The corresponding phase portrait illustrating the characteristic spiral behavior is shown in the inset in the right panel of Fig. 11.

In conclusion, we compare theoretical expression (66) with the density profile obtained in the AM with finite viscosity [86]. From (64), taking mass conservation into account, we find the following expression for the density:

$$\rho(x, D) = \frac{\rho_0 \cosh(x/\delta)}{\sqrt{\sinh^2(x/\delta) + \exp(-2UD/\delta)}}. \quad (71)$$

We focus on the asymptotic behavior at times $D \gg \delta/U$ and consider the regions $y > \delta$ and $x > \delta_p$, where $\delta_p = \delta \exp(-UD/\delta)$ is the internal scale of the clump. It is evident that in the adhesion approximation, the collapse occurs earlier than in the Q-model, and the spatial scale of the clump decreases as a power law of the effective BE ‘time’ $q_p \sim D^{-1/3}$. Analyzing the density profile for $|x| < \delta_p$, we find that the maximum density exponentially increases with time: $\rho_{\max}(0, D) = \rho_0 \exp(UD/\delta)$. Inside the interval $\delta_p \ll x \ll \delta$, the density distribution function is transformed into a time-independent power law $\rho(x, D) = \rho_0 \delta/x$, as is evident from Fig. 12, where the change in the spatial density distribution is shown as a function of the time $D = b$.

Thus, for a step-like initial velocity, at the late phase of the evolution, the AM shows localizations in the region $|x| < \delta = \text{const}$ and power-law tails, which cannot be integrated in time, with the characteristic size $\delta_s = \delta \exp(-Ub/\delta)$. We note that in the Q-model, by contrast, the integrated power-law tail is formed at the periphery [see (66)].

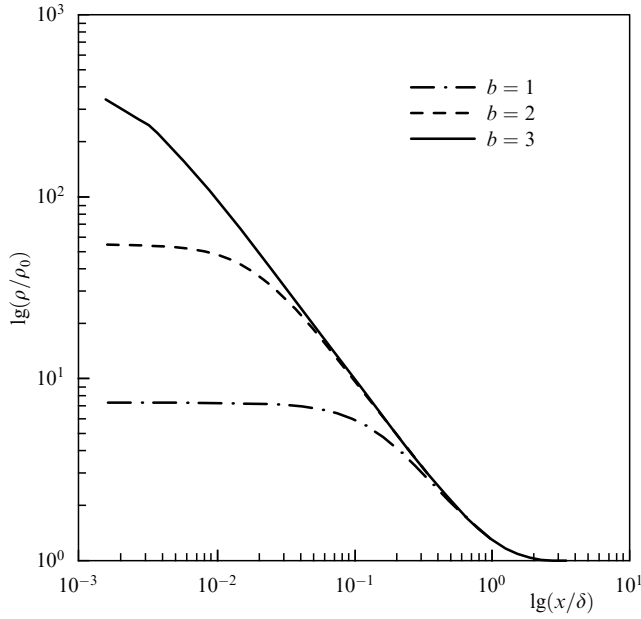


Figure 12. The normalized density ρ/ρ_0 versus x/δ in logarithmic scales for different values of the time b . The initial velocity is taken as a step-like function with the parameters $\delta = 5$, $U = 10$, and $\rho_0 = 1$.

It follows that in the one-dimensional case, the AM correctly describes the mass increase in clumps but not their internal structure. This is in line with the conclusion in [85], where numerical corrections to the diffusion coefficient are proposed and a new dynamical equation is introduced.

5.3 The general and asymptotic solutions of the vector Burgers equation

Below, we consider the BE in its classical form using the variable t instead of the effective time D :

$$\frac{\partial \mathbf{v}}{\partial t} + (\mathbf{v} \nabla) \mathbf{v} = \nu \nabla^2 \mathbf{v}. \quad (72)$$

We recall how BE (51) can be solved. For a potential velocity field, the BE is equivalent to the homogeneous Kardar–Parisi–Zhang (KPZ) equation for the velocity potential:

$$\frac{\partial \Phi}{\partial t} = \frac{1}{2} (\nabla \Phi)^2 + \nu \nabla^2 \Phi. \quad (73)$$

As in the one-dimensional case, using the Hopf–Cole substitution [80, 81]

$$\Phi(\mathbf{x}, t) = -2\nu \ln U(\mathbf{x}, t),$$

we arrive at the linear diffusion equation

$$\frac{\partial U}{\partial t} = \nu \nabla^2 U. \quad (74)$$

Substituting its solution in the expression for the velocity field

$$\mathbf{v} = -2\nu \nabla \ln U = -\frac{2\nu}{U} \nabla U,$$

we finally obtain

$$\mathbf{v}(\mathbf{x}, t) = \frac{\int d^3 q [(\mathbf{x} - \mathbf{q})/t] \exp [S(\mathbf{x}, t; \mathbf{q})/2\nu]}{\int d^3 q \exp [S(\mathbf{x}, t; \mathbf{q})/2\nu]}, \quad (75)$$

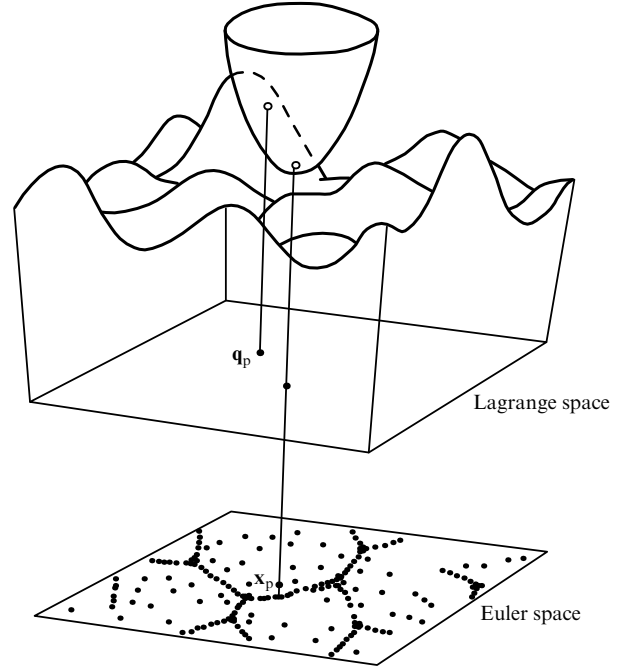


Figure 13. The connection of Lagrangian and Eulerian coordinates in AM.

where

$$S(\mathbf{x}, t; \mathbf{q}) = \Phi_0(\mathbf{q}) - \frac{(\mathbf{x} - \mathbf{q})^2}{2t} \quad (76)$$

is the action function.

We now discuss in more detail some consequences of the assumption about the infinitesimal viscosity coefficient, $\nu \rightarrow 0_+$, because this case is directly related to the formation of the mosaic large-scale structure of the Universe discussed in Section 1.

The integrals in (75) can be calculated using the steepest descent method [20, 37, 87, 88]. The velocity field is then given by

$$\mathbf{v}(\mathbf{x}, t) = \frac{\mathbf{x} - \mathbf{q}(\mathbf{x}, t)}{t}, \quad (77)$$

where $\mathbf{q}(\mathbf{x}, t)$ is the coordinate of the absolute minimum of the action $S(\mathbf{x}, D; \mathbf{q})$ at given values of \mathbf{x} and t . Here, $\mathbf{q}(\mathbf{x}, t)$ is the Lagrange coordinate of the particle that arrives at the point \mathbf{x} at time t [42].

In the two-dimensional case, the result of integration has a lucid geometrical interpretation (Fig. 13). The relation between the initial Lagrangian coordinates \mathbf{q}_p and the current Eulerian coordinate \mathbf{x}_p of a fixed particle at time t can be determined by dropping the paraboloid

$$P(\mathbf{q}; \mathbf{x}_p, t) = \frac{(\mathbf{x}_p - \mathbf{q})^2}{2t} + P_0 \quad (78)$$

on the surface of the initial potential. Specifically, we decrease the value of the constant P_0 from infinity until the paraboloid first touches the initial potential surface $\Phi_0(q)$ at some point with coordinates \mathbf{q}_p . Then the coordinates \mathbf{q}_p of the first tangency point are equal to the Lagrange coordinates of the particle.

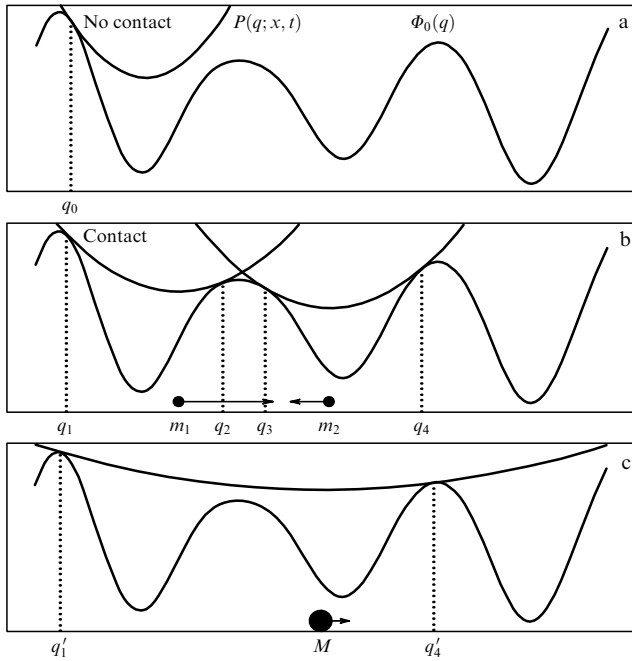


Figure 14. One-dimensional illustration of the procedure of finding the transformation from Lagrangian to Eulerian coordinates of particles by the scanning parabola method. The parabola apex drops onto the velocity potential curve. (a) A particle with the Lagrangian coordinate q_0 has the Eulerian coordinate x equal to the coordinate of the parabola apex. (b) At a later stage of particle motion, all particles with Lagrangian coordinates from the intervals (q_1, q_2) and (q_3, q_4) between points of double tangency of the parabolas stick to form macroparticles (the two black circles in the bottom part of the figure) with masses $m_1 = \bar{\eta}(q_2 - q_1)$ and $m_2 = \bar{\eta}(q_4 - q_3)$, moving with the velocities shown by arrows. (c) A macroparticle (the black circle) formed by merging the macroparticles shown in panel b (see [42, 89]).

We also note that in the early stage, the time t is small and the curvature of the paraboloid is significantly larger than the characteristic curvature of the surface Φ_0 . At this stage, the map of Lagrangian into Eulerian coordinates is almost everywhere equivalent to the ZA.

The curvature of the paraboloid decreases with time. Correspondingly, in the Lagrangian space, regions emerge that cannot be mapped on the Eulerian plane. This is evident from Fig. 14 illustrating the above procedure of the paraboloid dropping. The parabolas in Fig. 14b cannot be dropped without crossing the plot of Φ_0 . This means that particles with the initial Lagrangian coordinates located between two points of tangency of the parabola with coordinates q_1 and q_2 , as well as between the points with coordinates q_3 and q_4 , coalesce to form discrete macroparticles with masses $m_1 = \bar{\eta}(q_2 - q_1)$ and $m_2 = \bar{\eta}(q_4 - q_3)$. At the later stage, macroparticles become more massive because of the coalescence of particles formed earlier. Figure 14c shows such a massive macroparticle formed after the merging of macroparticles shown in Fig. 14b. It is easy to see that to transit from the stage shown in Fig. 14b to the stage shown in Fig. 14c, it is necessary that the parabola have three points of tangency with the plot of the initial potential at some intermediate time (i.e., for some intermediate value of the parameter D). At the next instant, the parabola becomes somewhat wider and loses contact with the initial potential profile at the middle tangency

point, which geometrically signals the merging of the colliding particles.

In the two-dimensional case, paraboloid (78) can touch the surface of the initial potential Φ_0 at one, two, or three points. The first type of contact corresponds to particles that have not merged by the given instant and have a finite density. Points of the second class of contact correspond to particles that coalesce along the line; these are two-dimensional analogs of Zeldovich pancakes. Particles on the coalescence line are shown in Fig. 14 by black circles with arrows indicating the particle velocities. These lines form boundaries of regions containing points of the first type and represent the locus of centers of parabolas touching the surface of the initial potential at two points simultaneously. Finally, when the paraboloid touches the surface of the initial potential at three points simultaneously, the coordinates of the centers of such parabolas correspond to the nodes connecting the lines described above. The lines and nodes form a chaotic mosaic structure consisting of cells bounded by the lines and nodes joining different lines. Some cells expand with time, while others contract and disappear. At the instant of cell merging, the paraboloid touches the initial potential at four points simultaneously. The classification of the features and their metamorphosis is described in [90].

5.4 Flows of locally interacting particles and a singular density field

There is an alternative way to calculate the matter density using the Jacobian of the transformation from Eulerian to Lagrangian coordinates [42, 43, 45, 91–94]. As long as there are no particle collisions occur, the density calculated in such a way corresponds to that in the ZA. But after coalescence, the function $\mathbf{q}(\mathbf{x}, t)$ has discontinuities at singularities of different dimensions. In the three-dimensional case, these include planes, lines, and points. Correspondingly, in the density distribution, singularities in the form of delta-functions of different dimensions appear [45, 91].

Below, we interpret Eqn (12) as an equation for the velocity field of some particle flow. As long as the solution of this equation is single valued, the field $\mathbf{v}(\mathbf{x}, t)$ bears the clear physical meaning of the hydrodynamic velocity of a uniformly moving flow of particles. Starting from some time instant t_n , some particles start overtaking others, and, if the particles do not interact with each other, a multi-stream flow occurs. By contrast, if the overtaking particles interact and prevent the formation of a multi-stream flow, then, instead of multi-stream fields, discontinuous one-stream fields $\mathbf{v}_w(\mathbf{x}, t)$ can appear, which we call weak solutions of Eqn (77).

For a one-dimensional flow, the mechanical interpretation of the formation of weak solutions due to inelastic particle coalescence is absolutely clear, but in the multi-dimensional case, it is difficult to propose the physical mechanism of the interaction leading to a relatively simple mathematical algorithm of the weak solution choice. We therefore consider the problem of particle interaction purely formally by postulating that the local interaction during collisions yields a discontinuous map $\mathbf{y} = \mathbf{y}_w(\mathbf{x}, t)$ of Eulerian coordinates to Lagrangian ones and, correspondingly, a weak solution for the velocity field of particles, which follows from the absolute maximum principle and the limit solution of the BE with infinitesimal viscosity.

We illustrate this model approach by analyzing the generalized density field $\rho_w(\mathbf{x}, t)$ of a two-dimensional flow of particles locally interacting during the overtaking. The flux

density can be written in the form

$$\rho_w(\mathbf{x}, t) = \rho_0 \int_{-\infty}^{\infty} \delta(\mathbf{X}_w(\mathbf{y}, t) - \mathbf{x}) d^2 y, \quad (79)$$

where $\mathbf{x} = \mathbf{X}_w(\mathbf{y}, t)$ is the map inverse to $\mathbf{y} = \mathbf{y}_w(\mathbf{x}, t)$, which in this case follows from the absolute minimum principle. In addition, we assume for simplicity that the initial density of gas interacting in accordance with the absolute minimum law is the same at any point \mathbf{x} of the plane: $\rho_0(\mathbf{x}) = \rho_0 = \text{const}$. As long as $\mathbf{y} = \mathbf{y}_w(\mathbf{x}, t)$ is a continuous function, this density coincides with that calculated using the ZA.

In the general case, $\rho_w(\mathbf{x}, t)$ is a singular generalized function. We explain the algorithm of its action on a trial function $\phi(\mathbf{x})$. After straightforward manipulations, we obtain

$$\int_{-\infty}^{\infty} \phi(\mathbf{x}) \rho_w(\mathbf{x}, t) d^2 x = \rho_0 \int_{-\infty}^{\infty} \phi(\mathbf{X}_w(\mathbf{y}, t)) d^2 y. \quad (80)$$

To use expression (80), we need to find means for constructing the function $\mathbf{x} = \mathbf{X}_w(\mathbf{y}, t)$. It is easy to show that the transformation from Lagrangian coordinates to Eulerian coordinates is determined by the expression [43, 45, 91]

$$\mathbf{x} = \mathbf{X}_w(\mathbf{y}, t) = -\nabla \bar{\varphi}(\mathbf{y}, t), \quad (81)$$

where $\bar{\varphi}(\mathbf{y}, t)$ is the convex hull of the function

$$\varphi(\mathbf{y}, t) = h_0(\mathbf{y}) t - \frac{y^2}{2}.$$

To obtain the convex hull of a function $\varphi(\mathbf{y}, t)$, it is necessary, figuratively speaking, to pull an elastic film over the values of $\varphi(\mathbf{y}, t)$. The film surface then represents the convex hull of $\varphi(\mathbf{y}, t)$.

The geometric construction of map (81) reduces to finding a plane touching the convex hull $z = \bar{\varphi}(\mathbf{y}, t)$ at the point with coordinates \mathbf{y} . We discuss this procedure in more detail. Let \mathbf{r} be the radius vector in three-dimensional space (\mathbf{y}, z) . The equation for the tangent plane has the form

$$\mathbf{n}(\mathbf{r} - \mathbf{a}) = 0, \quad \mathbf{a} = \{\mathbf{y}, \bar{\varphi}(\mathbf{y}, t)\},$$

where \mathbf{n} is the external normal vector to the convex hull $z = \bar{\varphi}(\mathbf{y}, t)$ (considering the region below the hull as its interior). We choose the z component of the normal to be unit everywhere, $\mathbf{n}_z = 1$. Then the projection of the normal onto the \mathbf{y} plane is equal to the sought vector $\mathbf{X}_w(\mathbf{y}, t)$. In other words, we find the map $\mathbf{x} = \mathbf{X}_w(\mathbf{y}, t)$ by specifying the normal \mathbf{n} at each point of the surface $z = \bar{\varphi}(\mathbf{y}, t)$ and projecting it onto the \mathbf{y} plane.

There are three robust types (which do not disappear at small displacements of the surface) of contact of a plane and a convex hull, which determine qualitatively different parts of map (81). Correspondingly, the Lagrangian \mathbf{y} and Eulerian \mathbf{x} planes are divided into three types of regions.

We enumerate the contact types and explain their mechanical interpretation in application to density field (79) of matter interacting during overtaking.

(1) The plane is in contact with the convex hull at one point. All such points belong to both the convex hull $\bar{\varphi}(\mathbf{y}, t)$ and the original surface $\varphi(\mathbf{y}, t)$. Projections of these points onto the plane \mathbf{y} are Lagrangian coordinates of particles of

the flow that have not yet participated in the interaction, and their Eulerian coordinates $\mathbf{x} = \mathbf{X}_w(\mathbf{y}, t)$ are specified by the map

$$\mathbf{x}(\mathbf{y}, t) = \mathbf{y} + t \mathbf{v}_0(\mathbf{y}) \quad (82)$$

for noninteracting particles.

(2) The plane is in contact with the original surface $\phi(\mathbf{y}, t)$ at two points simultaneously. Then the whole segment l connecting these two points belongs to the convex hull $\bar{\phi}(\mathbf{y}, t)$. Therefore, at all points of the segment, the normal vector to the convex hull is the same. This means that all points of the projection l_y of the segment l onto the Lagrangian plane \mathbf{y} are mapped into one point with the same Eulerian coordinates $\mathbf{x} = \mathbf{X}_w(\mathbf{y}, t)$. By sliding the tangent plane covered with chalk over the convex hull and trying to make the plane contact the hull at two points simultaneously, we draw a closed region \mathbb{G} on the hull. All points of its projection onto the plane \mathbb{G}_y are projected on the curve

$$\mathcal{L} = \{\mathbf{x} = \mathbf{X}_w(\mathbf{y}, t) : \mathbf{y} \in \mathbb{G}_y\},$$

in the Eulerian plane \mathbf{x} , where all matter originally located inside the region $\mathbf{y} \in \mathbb{G}$ is concentrated at the instant t .

(3) The plane is in contact with the surface at three points. After connecting them by line segments, we obtain a triangle \mathbb{T} ; the projection of all its points \mathbb{T}_y onto the Lagrangian plane \mathbf{y} are mapped into one point:

$$x^* = \{\mathbf{x} = \mathbf{X}_w(\mathbf{y}, t) : \mathbf{y} \in \mathbb{T}_y\}.$$

The partition of the Lagrangian plane \mathbf{y} into three types of regions and the singularities of their map onto the Eulerian plane \mathbf{x} are illustrated in Fig. 15. In the appendix to the English edition of book [42] (the authors of the Appendix are V I Arnold, Yu M Baryshnikov, and I A Bogaevsky), the classification of singularities and their bifurcations for two- and three-dimensional potential flows are given. The considered map exactly corresponds to such flows.

Three types of maps discussed above determine the structure of the generalized density field:

$$\rho(\mathbf{x}, t) = \hat{\rho}(\mathbf{x}, t) + \sum_i \varrho_i \delta_{\mathcal{L}_i} + \sum_j m_j^* \delta(\mathbf{x}_j^* - \mathbf{x}). \quad (83)$$

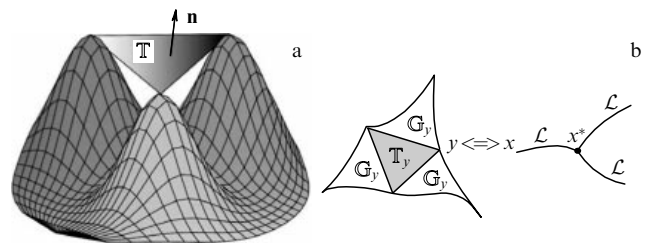


Figure 15. (a) A characteristic fragment of the surface $z = \varphi(\mathbf{y}, t)$ with three peaks. The points of contact of the surface with the tangent plane form the vertices of the triangle \mathbb{T} . The interior of the projection \mathbb{T}_y of the triangle onto the Lagrangian plane \mathbf{y} is mapped into one point x^* of the Eulerian plane. Troughs bounded by the double contact lines of the surface with the tangent plane go from the sides of the triangle; they are projected into lines \mathcal{L} on the Eulerian plane. (b) The geometry of the aforementioned regions in the Lagrangian and Eulerian planes.

The first term in the right-hand side of Eqn (83),

$$\hat{\rho}(\mathbf{x}, t) = \left\{ \frac{\rho_0}{J(\mathbf{y}(\mathbf{x}, t), t)} \right\},$$

describes the regular density of particles moving uniformly until the instant t . This term contains the Jacobian $J(\mathbf{y}, t)$ of the transformation (21) from Lagrangian to Eulerian coordinates, as well as the inverse transformation $\mathbf{y}(\mathbf{x}, t)$. The curly brackets mean that this expression is valid only in regions of the first type. In type-two and three regions, which have measure zero in the Eulerian plane, the definition of the expression in brackets must be refined by introducing any bounded functions.

The last term in the right-hand side of Eqn (83) yields a singular component of the density supported at type-three points x^* , where the matter from the triangle regions \mathbb{T}_y of the Lagrangian plane is concentrated. The coefficients at the delta-functions are equal to the mass of matter originally located in the triangles \mathbb{T}_y . If, as we believe, the initial density of the considered two-dimensional flow is everywhere equal to ρ_0 , then

$$m^* = \rho_0 S_{\mathbb{T}},$$

where $S_{\mathbb{T}}$ is the area of the corresponding triangle \mathbb{T}_y .

We separately consider the second term in the right-hand side of Eqn (83), which is equal to the sum of linear delta-functions corresponding to type-two regions \mathbb{G}_y . The linear delta-function acts on a test function $\phi(\mathbf{y})$ as

$$\int_{-\infty}^{\infty} \phi(\mathbf{x}) \varrho \delta_{\mathcal{L}} d^2x = \int_{\mathcal{L}} \varrho(\sigma, t) \phi(\mathbf{x}(\sigma)) d\sigma. \quad (84)$$

In other words, the linear delta-function $\delta_{\mathcal{L}}$ ‘cuts out’ the contour integral of the first type along the curve \mathcal{L} from the double integral. The integrand is the linear density ϱ of the material line \mathcal{L} times the test function $\phi(\mathbf{x})$. The integral is written using the parametric equation $\mathbf{x} = \mathbf{x}(\sigma)$ of the curve \mathcal{L} , where σ is the natural parameter equal to the curve length counted from some initial point.

To find the linear density $\varrho(\sigma, t)$ on the curve \mathcal{L} , we take an infinitely short segment $[\sigma, \sigma + d\sigma]$. The subarea $d\mathbb{G}_y$ of the domain \mathbb{G}_y , collapsing into the curve \mathcal{L} of the Eulerian plane is mapped into this segment. The subarea $d\mathbb{G}_y$ is bounded by the intervals $l_y(\sigma, t)$ and $l_y(\sigma + d\sigma, t)$, which are mapped into the ends of the segment $[\sigma, \sigma + d\sigma]$. The sought linear density is then

$$\varrho(\sigma, t) = \lim_{d\sigma \rightarrow 0} \frac{dm(\sigma)}{d\sigma},$$

where $dm(\sigma)$ is the mass of matter originally found in the subarea $d\mathbb{G}_y$.

5.5 The web-like structure in the adhesion model

In this section, we compare the results obtained using the AM with direct numerical simulation of the motion of gravitationally interacting particles.

Figure 16 demonstrates a good agreement between the mosaic structure obtained in the AM framework and the results of numerical simulation of two-dimensional motion of gravitationally interacting particles. Figure 17 illustrates the effect of the power-law spectrum of initial perturbations on small scales. Initial perturbations in Fig. 17 are generated with equal amplitudes and phases, but the amplitudes of

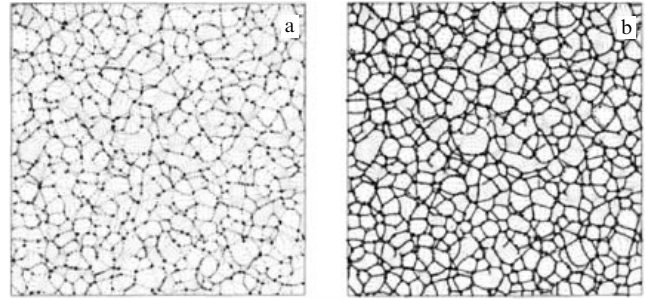


Figure 16. (a) The distribution of gravitationally interacting 2D particles found from numerical integration of their motion. (b) The chaotic mosaic structure obtained in the 2D version of the AM superimposed on the particle distribution shown in panel (a) [88].

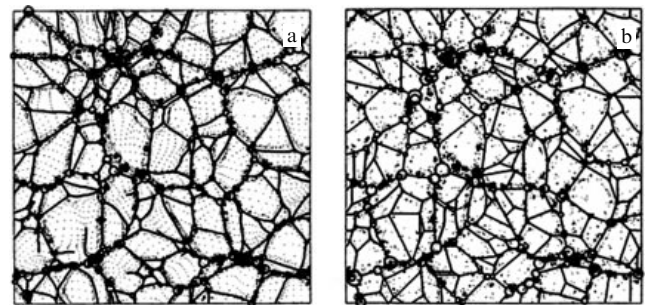


Figure 17. Plane mosaic structures obtained in the AM, superimposed on the particle distribution in the 2D N -body problem. For images a and b, the initial potential Φ_0 has the same large-scale structure, but in image a, Φ_0 is smoothed by a cut-off removing short-scale components, which are taken into account in image b [88].

harmonics with wavelengths $k > k_{\text{cr}}$ are taken to be zero in Fig. 17a. Correspondingly, the initial potential in Fig. 17a is a smoothed version of that in Fig. 17b. Both Fig. 17a and b correspond to the same stage of evolution of the large-scale structure of the Universe (to the same value of the parameter D). It is evident that although the general character of the structure in Fig. 17a and b is nearly the same, the mosaic in Fig. 17b demonstrates a much richer small-scale structure.

Based on two-dimensional geometrical constructions considered in Sections 5.3 and 5.4, it is straightforward to understand the basic features of the mosaic structure of the large-scale 3D matter distribution. Namely, the initial potential Φ_0 represents a three-dimensional hypersurface in a four-dimensional space. Correspondingly, as in the one- and two-dimensional cases described above, three-dimensional paraboloid (78) drops onto the initial potential hypersurface. The rules to find the transformation from Lagrangian to Eulerian coordinates remain the same: these are coordinates of the points of the first contact between the paraboloid and the initial potential surface and the coordinates of the paraboloid apex. There are four types of contact between the paraboloid and the initial potential.

If the paraboloid is in contact with the initial potential at only one point, then the corresponding particle has not collided with other particles until the current instant (the value of the parameter D). In the other three cases where the paraboloid is in contact simultaneously at two, three, or four points with the initial potential, the paraboloid apex

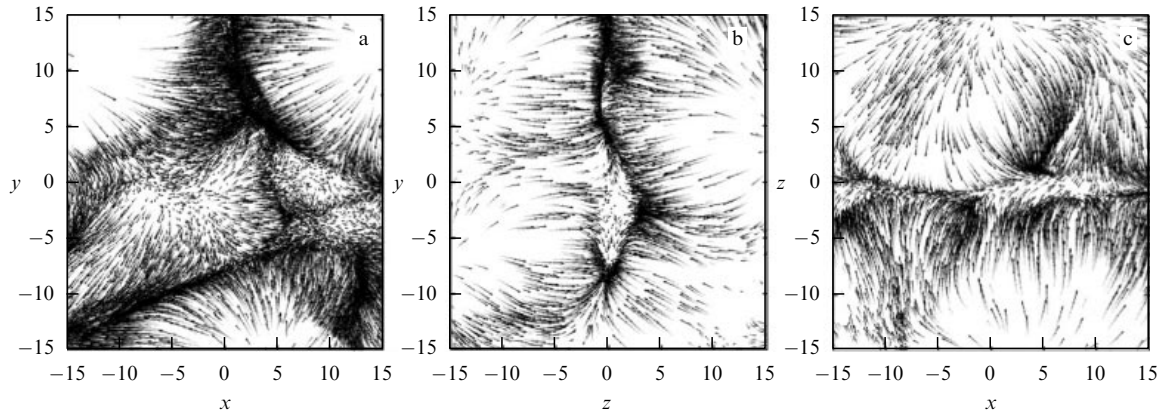


Figure 18. 3D dynamics of the AM. The matter falling onto a pancake is shown in three orthogonal projections; (a) the xy projection demonstrates the motion of particles in the pancake plane [71].

corresponds to particles respectively merged on faces, edges, or vertices of a three-dimensional mosaic structure. Moreover, as in the one- and two-dimensional cases, at critical times corresponding to the disappearance of some cells of the three-dimensional mosaic structure, the number of tangency points of the paraboloid and the initial potential becomes larger than four [90]. The set of surfaces (pancakes), massive lines, and compact clusters determines the mosaic structure of the 3D matter distribution, in which matter is mainly concentrated at the mosaic boundaries—in massive pancakes, filaments, and vertices separating mosaic cells (low-density voids). This three-dimensional mosaic structure serves as the backbone of the real matter distribution in the Universe.

The adhesion model reveals a nontrivial structure of quasi-2D walls surrounding cells. Particles entering the walls continue moving inside them, which in turn leads to the formation of a 2D web-like structure in the walls themselves [71]. In Fig. 18a, where the wall is shown face-on, two-dimensional cells of different sizes are clearly seen.

The two variants of the AM mentioned above were tested by comparing the results of numerical modeling of the 2D and 3D gravitational N -body problem [59, 69–71, 79, 88]. The same boundary conditions were used and the comparison was made at different stages of the gravitational instability development. In addition, the geometrical version ($v \rightarrow 0_+$) of the AM was compared with 2D N -body simulations for the initial power-law spectrum $P_\delta(k) \propto k^n$ with different exponents $n = 2, 0, -2$ and different critical cut-off wavenumbers above which the spectrum P was set to zero [88].

It turned out that at a small but nonzero viscosity coefficient $\nu > 0$, the AM both qualitatively and quantitatively agrees with numerical N -body simulations at the strongly nonlinear stage of gravitational instability [69]. In general, the comparison of matter density distributions obtained in the numerical simulations and adhesion models demonstrate good agreement, which improves with increasing the steepness of the initial power spectrum on large scales typical for the Λ CDM model (see Fig. 5). Figure 6 clearly illustrates this fact.

Correlations of the initial potential peaks with the cell diameters of the structure were studied in [69]. In the three-dimensional numerical AM, cells were identified inside which the initial potential peaks were found. Figure 19 demonstrates the obvious correlation between the cell diameter and the

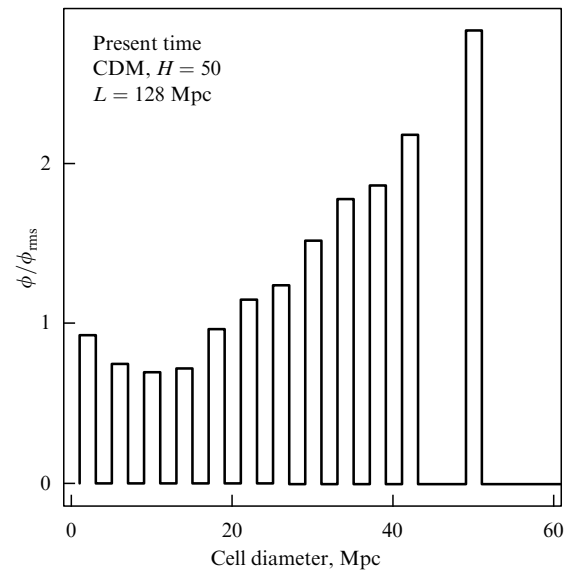


Figure 19. The normalized initial gravitational potential at centers of the mosaic cells (dark voids) as a function of the cell diameter [89].

initial potential peak amplitude inside it. Figure 20, obtained in the two-dimensional case [95], clearly confirms this result.

5.6 Particle dynamics inside velocity field discontinuities in the Hamilton–Jacobi equation

In the limit case of infinitesimal viscosity, the dynamics of three-dimensional motion (52) were studied in papers [96, 97], which showed a nontrivial behavior of particles in singularities of the velocity field. In particular, under certain conditions, the clumps can leave the nodes of the structure. Below, we present the main results of the above paper and other papers on this topic. The material for this section was kindly provided by A N Sobolevsky.

In the multi-dimensional case, the BE $\partial_t \mathbf{v} + (\mathbf{v} \nabla) \mathbf{v} = 0$ for a vortex-free velocity field $\mathbf{v}(t, \mathbf{r})$, i.e., $\mathbf{v} = \nabla \phi$, is equivalent to the equation

$$\partial_t \phi + \frac{1}{2} |\nabla \phi|^2 = 0. \quad (85)$$

It is known from mechanics that the function of action ϕ of a general Hamiltonian system with a Hamiltonian $H(t, \mathbf{r}, \mathbf{p})$, where \mathbf{p} is the generalized momentum vector, satisfies the

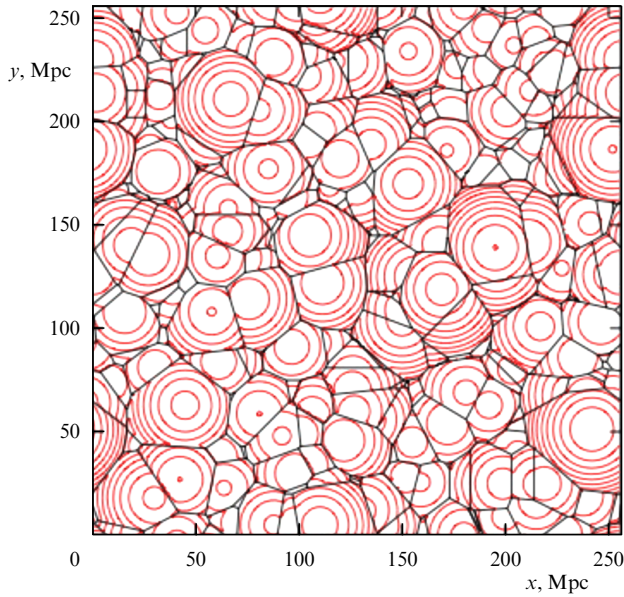


Figure 20. 2D model of the web-like structure obtained with the potential shown in light (red) curves, the so-called quasi-Voronoi tessellation [95].

Hamilton–Jacobi equation

$$\partial_t \phi + H(t, \mathbf{r}, \nabla \phi) = 0. \quad (86)$$

In particular, the Hamiltonian $H(\mathbf{p}) = |\mathbf{p}|^2/2$ corresponds to Eqn (85).

Below, we consider a general Hamiltonian $H(t, \mathbf{r}, \mathbf{p})$ under the assumption that as a function of \mathbf{p} , it never turns to infinity and is smooth and strictly convex at all points. This allows establishing a one-to-one correspondence between momenta and velocities, $\mathbf{v} = \nabla_{\mathbf{p}} H(t, \mathbf{r}, \mathbf{p})$, and introducing the Lagrangian $L(t, \mathbf{r}, \mathbf{v}) = \mathbf{p}\mathbf{v} - H(t, \mathbf{x}, \mathbf{p})$, where $\mathbf{p} = \nabla_{\mathbf{v}} L(t, \mathbf{r}, \mathbf{v})$.

Our task is to give Hamilton–Jacobi equation (86) a hydrodynamic interpretation by using its relation with the BE. For this, we associate a solution ϕ of this equation with a flow in which the particle, which is at the point \mathbf{r} at time t , moves with the velocity

$$\dot{\mathbf{r}} = \nabla_{\mathbf{p}} H(t, \mathbf{r}, \nabla \phi(t, \mathbf{r})). \quad (87)$$

Relation (87) is one of the canonical Hamilton equations, in which the gradient of ϕ is used instead of momentum.

Definition (87) of particle velocities is valid everywhere where the solution ϕ of Eqn (86) is differentiable. However, due to the nonlinearity of the Burgers equation, discontinuities at which the velocity is undefined appear in its solutions. Similar singularities (discontinuities of the gradient of ϕ) also emerge in solutions of the general Hamilton–Jacobi equation (86). Therefore, it is necessary to separately construct the particle dynamics ‘inside discontinuities’ of the solution.

In the $(1+1)$ -dimensional time–space, such a construction is straightforward. As is well known, the velocity of a discontinuity point $x(t)$ in the ‘correct’ solution of the BE always satisfies the conditions $v(x(t)-0, t) > \dot{x}(t) > v(x(t)+0, t)$, i.e., the flow ‘deposits’ particles on both sides of the discontinuity, where they stay forever. The same conditions are valid for solutions of the general Hamilton–Jacobi equation with a convex Hamiltonian. Therefore, in the

one-dimensional case, particles settled into a discontinuity do not leave it and continue moving with the discontinuity.

In the multi-dimensional case, the geometry of the flow near a discontinuity is also such that particles are ‘deposited’ on the discontinuity; however, the set of discontinuity points (‘the manifold of discontinuities’) is more complicated than in the one-dimensional case and represents a union of smooth pieces of different dimensions: in two dimensions, discontinuities occur along curves whose ends are connected at points with triple and higher-order multiplicities, and in three dimensions, discontinuity surfaces appear, which are connected by lines ending at points with quadruple or higher-order multiplicities.

Hence, particles deposited on the discontinuity preserve the degrees of freedom inside it, and the determination of their motion inside the discontinuity manifold remains a nontrivial problem.

For the BE (or, equivalently, for the Hamilton–Jacobi equation with a quadratic Hamiltonian), this problem was first solved by Bogaevsky [96, 98]. Part of his results were anticipated in earlier work by Brézis [99] (see also [100], lemma 5.6.2), but these papers remained unfamiliar to specialists in nonlinear acoustics and hydrodynamics. Moreover, Bogaevsky first classified pieces of the discontinuity manifold depending on whether they retain the deposited particles or the particles can pass into pieces with a higher dimension.

The methods in [96, 98–100] essentially use quadratic Hamiltonians. We here use another approach: the general convex Hamiltonian is considered and the presentation follows papers by Sobolevsky and Khanin [97, 101].

We recall that the solution of Hamilton–Jacobi equation (86) satisfying the initial condition $\phi(t=0, \mathbf{r}) = \phi_0(\mathbf{r})$ can be presented in the form manifesting the least action principle:

$$\phi(t, \mathbf{r}) = \min \left[\phi_0(\gamma(0)) + \int_0^t L(s, \gamma(s), \dot{\gamma}(s)) ds \right],$$

where the expression in square brackets is the Lagrangian action along the trajectory γ , taking the initial value ϕ_0 into account, and the minimum is calculated over all trajectories satisfying the condition $\gamma(t) = \mathbf{r}$.

At most points of the space–time, this minimum is reached on one trajectory and the solution ϕ is differentiable. But at some points, the same minimum value of the action corresponds to several trajectories γ_i that have different origins and different velocities at time t . Exactly these points make the set of the velocity field discontinuities corresponding to the solution ϕ in accordance with formula (87).

In the vicinity of such a point (t, \mathbf{r}) , the solution ϕ can be represented as the minimum of several smooth functions ϕ_i , each of which is determined by the initial condition ϕ_0 near the corresponding initial point $\gamma_i(0)$:

$$\begin{aligned} \phi(t', \mathbf{r}') &= \min_i \phi_i(t', \mathbf{r}') \\ &= \phi(t, \mathbf{r}) + \min_i [\nabla \phi_i(\mathbf{r}' - \mathbf{r}) + \partial_t \phi_i(t' - t)] + \dots, \end{aligned}$$

in the linear order of approximation.

At the point (t, \mathbf{r}) , the smooth functions ϕ_i intersect, and the values of the derivatives $\partial_t \phi, \nabla \phi$ are not defined. After the convolution with a smoothing kernel of size ϵ or after the introduction of a small viscosity ϵ into Eqn (86), the smoothed solution ϕ^ϵ in a small neighborhood of this point has

derivatives with values that fall between the limit values of $\partial_t \phi_i$ and $\nabla \phi_i$ corresponding to smooth branches of the solution ϕ_i . Therefore, it is natural to assume that for a nonsmooth function, such a neighborhood shrinks to the point (t, \mathbf{r}) in which the vector of derivatives $(\partial_t \phi, \nabla \phi)$ takes all values from a polyhedron—the convex hull of the set $\{(\partial_t \phi_i, \nabla \phi_i)\}$.

For brevity, we set $\mathbf{p}_i = \nabla \phi_i(t, \mathbf{r})$. Because ϕ_i are smooth functions satisfying the Hamilton–Jacobi equation in the vicinity of (t, \mathbf{r}) , we have $\partial_t \phi_i = -H(t, \mathbf{r}, \nabla \phi_i) = -H(t, \mathbf{r}, \mathbf{p}_i) = -H_i$, and the linear approximation for ϕ takes the form

$$\phi(t', \mathbf{r}') - \phi(t, \mathbf{r}) = \min_i [\mathbf{p}_i(\mathbf{r}' - \mathbf{r}) - H_i(t' - t)] + \dots$$

These calculations lead to a simple but important conclusion: if a trajectory goes out from the point \mathbf{r} with the velocity \mathbf{v} at time t , then at the infinitely close time instants $t' > t$, the solution in the immediate vicinity of the trajectory $\mathbf{r}' = \mathbf{r} + \mathbf{v}(t' - t)$ is determined not by all branches of ϕ_i but only by those whose indices belong to the set

$$I_{t, \mathbf{r}}(\mathbf{v}) = \arg \min_i [\mathbf{p}_i \mathbf{v} - H_i].$$

The ‘spectrum’ of momentum values along such a trajectory is specified by the convex hull of the corresponding momentum set $\text{conv} \{\mathbf{p}_i; i \in I_{t, \mathbf{r}}(\mathbf{v})\}$. By virtue of (87), these momenta correspond to velocities of the form $\mathbf{v}' = \nabla_{\mathbf{p}} H(t, \mathbf{r}, \mathbf{p}')$, where

$$\mathbf{p}' = \nabla_{\mathbf{p}} L(t, \mathbf{r}, \mathbf{v}') \in \text{conv} \{\mathbf{p}_i; i \in I_{t, \mathbf{r}}(\mathbf{v})\}.$$

We call the velocity \mathbf{v}^* *admissible* at a point (t, \mathbf{r}) if

$$\nabla_{\mathbf{p}} L(t, \mathbf{r}, \mathbf{v}^*) \in \text{conv} \{\mathbf{p}_i; i \in I_{t, \mathbf{r}}(\mathbf{v}^*)\}, \quad (88)$$

i.e., if \mathbf{v}^* corresponds to a momentum from the momentum ‘spectrum’ along the trajectory $\mathbf{r} + \mathbf{v}^*(t' - t)$.

It turns out that the admissible velocity is defined uniquely [97]. Indeed, it is straightforward to show that for \mathbf{v} satisfying condition (88), the strictly convex function

$$\hat{L}(\mathbf{v}) = L(t, \mathbf{r}, \mathbf{v}) + \max_i [H_i - \mathbf{p}_i \mathbf{v}] \quad (89)$$

reaches its only minimum. In particular, if the function ϕ is differentiable at (t, \mathbf{r}) , i.e., there is only one branch, then (88) reduces to the formula $\nabla_{\mathbf{p}} L(t, \mathbf{r}, \dot{\mathbf{r}}) = \nabla \phi(t, \mathbf{r})$, which is equivalent to (87). Therefore, it is not only at the discontinuities but also everywhere inside the flow corresponding to a nonsmooth solution ϕ of Hamilton–Jacobi equation (86) that the trajectory dynamics can be determined using the following generalization of canonical equation (87):

$$\dot{\mathbf{r}} = \mathbf{v}^*(t, \mathbf{r}), \quad (90)$$

where $\mathbf{v}^*(t, \mathbf{r})$ is found from the values $\nabla \phi_i(t, \mathbf{r}) = \mathbf{p}_i$ in accordance with condition (88).

The right-hand side of ordinary differential equation (90) involves a discontinuous velocity field, and therefore neither the existence nor uniqueness of its integral trajectories is evident. We consider a solution ϕ^ϵ smoothed out in some way and the corresponding flow of smooth trajectories determined by the equation

$$\dot{\mathbf{r}}^\epsilon = \nabla_{\mathbf{p}} H(t, \mathbf{r}^\epsilon, \nabla \phi^\epsilon(t, \mathbf{r}^\epsilon)).$$

It can be shown that the flow of integral trajectories of differential equation (90) with a discontinuous right-hand side can be constructed as the limit of smoothed trajectories: if a solution ϕ^ϵ converges to ϕ and \mathbf{r}^ϵ tends to \mathbf{r} as the smoothing parameter ϵ vanishes, then the one-sided derivatives $\dot{\mathbf{r}}^\epsilon(t+0)$ of the smoothed trajectories converge to the admissible velocity \mathbf{v}^* at the point (t, \mathbf{r}) .

We note that the constructed flow is irreversible: at points of the field velocity discontinuities characterized by the set of momenta $\mathbf{p}_i = \nabla \phi_i$, the one-sided derivative $\dot{\mathbf{r}}(t-0)$ can take any value $\nabla_{\mathbf{p}} H(t, \mathbf{r}, \mathbf{p}_i)$, but the derivative $\dot{\mathbf{r}}(t+0)$ is defined uniquely. For $i' \notin I_{t, \mathbf{r}}(\mathbf{v}^*)$, the full derivative of the branch $\phi_{i'}$ along the direction specified by the velocity \mathbf{v}^* is larger than analogous full derivatives for branches with indices $i \in I_{t, \mathbf{r}}(\mathbf{v}^*)$:

$$\dot{\phi}_{i'} = \partial_t \phi_{i'} + \mathbf{v}^* \nabla \phi_{i'} = \mathbf{p}_{i'} \mathbf{v}^* - H_{i'} > \min_i (\mathbf{p}_i \mathbf{v}^* - H_i).$$

Hence, the branch $\phi_{i'}$ does not contribute to the pointwise minimum $\min_i \mathbf{p}_i$ at $t' > t$, and the trajectory passing through the intersection point (t, \mathbf{r}) of many branches of the solution does not move together with this crossing but leaves it at $t' > t$ along the region of the discontinuity manifold of a higher dimension. This phenomenon was first noted in [96, 98].

However, even among the ϕ_i branches whose indices enter $I_{t, \mathbf{r}}(\mathbf{v}^*)$, generally speaking, there can be ‘extra’ branches. Indeed, if the admissible velocity \mathbf{v}^* is known, we can determine how the momentum configuration $\{\mathbf{p}_i(t')\}$ is deformed at small $t' - t > 0$ in the linear approximation. Under some additional assumptions about L , it is possible to show that the minimal set of solution branches, which determines the trajectory coming out from the point (t, \mathbf{r}) , consists of the trajectories that participate in the formation of the minimum with respect to \mathbf{v} of the function

$$\hat{L}(t', \mathbf{v}) = L(t', \mathbf{r} + \mathbf{v}^*(t' - t), \mathbf{v}) + \max_i [H_i(t') - \mathbf{p}_i(t') \mathbf{v}]$$

for sufficiently small $t' > t$ [cf. (89)]. This minimum set is uniquely determined and in turn defines a unique integral trajectory of Eqn (90) passing through the point (t, \mathbf{r}) in the forward direction in time. The proof of the existence and uniqueness of integral trajectories of Eqn (90) is thus completed.

6. Statistical properties of the potential turbulence: the Burgers vector turbulence

As noted in Section 5, vector BE (72) underlies the AM. Jointly with the equation for density, this equation is used to describe the large-scale structure formation of the Universe at the nonlinear stage of gravitational instability, when pressure forces can be neglected. In what follows, we therefore briefly discuss the statistical properties of the Burgers turbulence—the solution of Eqn (72) with random initial conditions. We consider only the case of a potential velocity field, typical for gravitational instability developments. The velocity field is treated as the field of potential turbulence.

The one-dimensional nonlinear diffusion equation

$$\frac{\partial v}{\partial t} + v \frac{\partial v}{\partial x} = \nu \frac{\partial^2 v}{\partial x^2} \quad (91)$$

was originally introduced by Burgers [38] as a model for hydrodynamic turbulence. Other problems leading to the

multi-dimensional BE or its variants include the growth of the medium boundary surface due to random sedimentation on the surface and the motion of the flame front [102]. In these cases, the potential ψ corresponds to the surface profile, and the equation describing its evolution is equivalent to KPZ equation (73) [102–105]. In problems of the growth of the interface between two media, v has the meaning of the surface tension coefficient, and the term in the right-hand side describes linear effects of surface smoothing. The surface roughness is measured by its root-mean square gradient:

$$E(t) = \langle (\nabla \psi(\mathbf{x}, t))^2 \rangle = \langle v^2(\mathbf{x}, t) \rangle = \sum_i E_i(t), \quad (92)$$

$$E_i(t) = \left\langle \left(\frac{\partial \psi}{\partial x_i} \right)^2 \right\rangle = \langle v_i^2 \rangle. \quad (93)$$

The angular brackets denote ensemble averaging or integration over the spatial coordinate (for a localized perturbation).

Before the formation of discontinuities, the multi-dimensional BE in the limit of vanishing viscosity is equivalent to the equation describing the free motion of particles. In the Lagrangian representation, the velocity of particles $\mathbf{V}(t; \mathbf{y})$ is constant and depends only on the initial (Lagrangian) particle coordinate \mathbf{y} . In the one-dimensional case, before the formation of discontinuities, an increase in the length of one elementary interval in the Eulerian representation $\Delta \mathbf{x} = \Delta \mathbf{y} + t \Delta \mathbf{V}$ is compensated by a decrease in the length of the adjacent interval $\Delta \mathbf{x} = \Delta \mathbf{y} - t \Delta \mathbf{V}$; hence, the energy of the wave is conserved. After the formation of discontinuities, the energy starts increasing with time. In the multi-dimensional case, the change of the elementary volume in the Eulerian representation depends on the initial curvature of the perturbed surface, and the compensation of expanding and contracting volumes does not occur. Therefore, for $d > 1$, the measure of surface roughness $E(t)$ in (92) can both increase and decrease with time [106, 107], which manifests the absence of any conservation law in this case. Nevertheless, we call $E(t)$ the ‘energy of turbulence’ and $E_i(t)$ the energy of the i th velocity component.

The dynamical and statistical properties of solutions of the one-dimensional (and recently, of three-dimensional) BE have been studied in many papers (see, e.g., the references in books [42, 45, 105, 108] and reviews [101, 109, 110]). In spite of the existence of an exact solution (the Hopf–Cole solution) of the BE, the analysis of deterministic—and especially random—fields is a very complicated mathematical problem. For example, first serious results for the Brownian initial potential [39] were obtained only 30 years after the appearance of the equation itself [38], and this special case was exactly described statistically quite recently [111].

The BE describes two main properties of any turbulence [112]: the nonlinear energy redistribution across the spectrum and the viscosity effect on small spatial scales. That is why the BE is of great interest for both direct physical applications and tests of different models of developed turbulence.

We note that the study of the Burgers turbulence with infinitesimal viscosity reduces to searching for statistical characteristics of coordinates of absolute maxima of the action $S(\mathbf{x}, t; \mathbf{q})$. The use of the limit theorems of the theory of random field fluctuations allows an almost complete description of the Burgers turbulence in both one- and multi-dimensional cases. For the Burgers turbulence, it is possible to find conditions for the existence and types of self-

similar modes of the turbulence degeneracy, spectra, correlation functions, and one-point and multi-point probability distributions (see, e.g., [36, 42, 43, 45, 91, 101, 107, 109, 111, 113–116]).

The occurrence of local and statistical self-similarity is a characteristic signature of turbulence evolution. A continuous initial field is transformed into a cellular structure, with each cell having the universal self-similar structure forming on large time scales [36, 42]:

$$\mathbf{v}(\mathbf{x}, t) = \frac{\mathbf{x} - \mathbf{y}_k}{t}. \quad (94)$$

Some cells engulf others as time passes, and the characteristic field scale increases. Because of multiple cell coalescences, the statistical properties of the turbulence also become self-similar.

When there are no long-range correlations of the initial field, the turbulence behavior at late times is determined by the ‘tails’ of the initial potential distribution function. Depending on the initial potential distribution, one of three universal self-similarity modes of the turbulence decay is then realized [115], and the ‘energy’ increase of the three-dimensional turbulence (92) is possible.

If the initial potential $\psi_0(\mathbf{x})$ is described by a random Gaussian field, the asymptotic behavior of the turbulence is determined by the initial form of the spectrum at small wave numbers, i.e., by large-scale field components. If these components are sufficiently representative in the initial spectrum, a self-similar turbulence regime is realized in which the outer scale increase is determined by the spectral shape at small wave numbers [42, 43].

If there are no large-scale components in the initial field, another self-similarity mode is realized [42, 115]. The increase in the outer scale $L(t) \sim t^{1/2}$ (with a logarithmic correction) is then determined by integral properties of the initial spectrum.

The spectral density $E(k, t)$ is also isotropic and self-similar:

$$E(k, t) = \frac{L^3(t)}{t^2} \tilde{E}(kL(t)).$$

At large wave numbers k , the formation of discontinuities (small-scale jumps) leads to the appearance of a power-law asymptotic dependence $\tilde{E}(k) \sim k^{-2}$. At small wave numbers in the three-dimensional case, the spectrum is also characterized by the universal behavior

$$E(k, t) = k^{d+1} \frac{L^{4+d}(t)}{t^2} \sim k^{d+1} t^{d/2},$$

suggesting nonlinear generation of the large-scale component corresponding to small wave numbers.

For example, in the case of three-dimensional Burgers turbulence, $E(k, t) \sim k^4 t^{3/2}$. At large but finite Reynolds numbers, the discontinuities have a finite width $\delta \sim \mu t / L(t)$ and increase with time compared with the integral scale as $\delta / L(t) \sim (\ln(\sigma_\psi t / t_{\text{eff}}^2))^{1/2}$. For this reason, the linear stage of the evolution begins on very long time scales.

In the three-dimensional Burgers turbulence, as in the one-dimensional case [114, 115], it is possible to violate the global statistical self-similarity: at small wave numbers, the spectrum is preserved, but the evolution of most of the spectrum has a universal character and is determined by integral characteristics of the initial spectrum.

7. Conclusion

Concluding the discussion of different formation models of the large-scale structure of the Universe, we emphasize that the adhesion model based on three-dimensional BE (51) gives a visual interpretation of the formation of the basic properties of the large-scale matter distribution and quantitatively (although approximately) agrees with cosmological observations of the large-scale structure of the Universe. The limit version of the AM corresponding to $v \rightarrow 0_+$ leads to a natural geometrical construction of the large-scale structure ‘skeleton’, which can be characterized as a ‘quasi-Voronoi tessellation’ [44, 117]. The comparison of the AM predictions with 1D, 2D, and 3D N -body simulations demonstrates good agreement at all stages, including the stage of the strongly nonlinear gravitational instability development.

Therefore, the AM can naturally explain the formation of coherent large-scale structures, including massive sheets (Zeldovich pancakes), filaments, and compact clumps of matter, as the result of matter density evolution due to small fluctuations of the initial gravitational potential.

We stress that the values of the initial gravitational potential are closely related to the details of the emerging large-scale structure, as can be seen in Fig. 17: the higher the initial potential peak is, the larger the size of the mosaic structure cell around it (also see Fig. 6.2 in [95]). The formation and later evolution of the large-scale structure is described by the AM as a two-stage process [89, 119].

At the first stage, matter is concentrated in pancakes and then moves inside them toward massive lines—edges of the emerging structure, motion along which leads to the formation of vertices—massive compact clumps in the vicinity of intersecting edges. In the currently popular Λ CDM model, this stage is characterized by a minuscule (in cosmological terms) scale determined by the type of dark matter assumed in one model or another. For example, if dark matter consists of hypothetical neutralinos with the mass of the order of 100 GeV, then the characteristic mass of first structures is only of the order of Earth’s mass (see, e.g., [119]). By the end of the first stage, the mosaic structure of matter distribution is completed, in which most of the matter is concentrated in edges and vertices of the structure, and only a small proportion remains in the pancakes and in dark volumes inside individual cells. This stage has not been numerically studied yet because it requires a huge number of particles to be included into the model, which is currently unfeasible.

The second stage is characterized by a deformation of the mosaic structure due to the gravitational interaction of matter. At this stage, some cells become increasingly massive and large, while others shrink and disappear, being engulfed by larger cells. Ultimately, almost all of the matter mass is mainly concentrated in gravitationally bound compact dark matter clusters, ranging from the lowest-mass ones that were formed at the first stage to very large ones, which are naturally associated with massive galaxy clusters. Such compact clusters of dark matter are referred to as dark matter halos. Halos corresponding to galaxy masses gravitationally attract the baryonic mass component, and stars are formed there; the halos thus turn into galaxies. Halos with larger masses can form groups of galaxies and galaxy clusters.

In the commonly accepted model of the Universe, the initial spectrum of perturbations is such that dark halos, in turn, move coherently by concentrating along super-

pancakes and super-filaments, such that the edges and faces of the structure at this stage occur as regions with an enhanced concentration of dark halos with various masses. Such a scenario of the evolution of the large-scale structure is characteristic for the present-day matter distribution in the standard cosmological model. The initial spectrum of perturbations in this model is shown in Fig. 5, and the power density spectrum of the initial gravitational potential is obtained by multiplying the density spectrum by k^{-4} . Super-pancakes and super-filaments can be identified in the AM framework with a smoothed initial potential [88]. The mass flow from the inner volume of cells to faces, from faces to edges, and from edges to vertices remains, as a whole, the same as in the first stage, which is confirmed by observations [21, 22].

In the currently recognized model of the Universe (Λ CDM), as the expansion rate accelerates at small z , the linear increase of perturbations slows down: for example, at $z = 0.6$ and at the present time, the respective linear function of perturbation growth is about 90% and 75% of that in the Einstein–de Sitter model at the corresponding epochs. In a short time (on the cosmological scale), the linear perturbation growth should almost stop and structures that have reached virial equilibrium will evolve as independent island universes that run away with exponentially increasing velocities. The modern structure of the Universe has therefore almost reached the largest scale and will not grow in the future.

Numerical simulations of the present-day structure of the Universe typically have the resolution corresponding to masses of sufficiently large galaxies, whose redshifts can be measured in large sky surveys like SDSS and compared with the results of simulations. In such numerical models, the structure is inevitably ‘smoothed’ on small scales. In particular, the dark matter density field in dark voids with no galaxies turns out to be unrealistically smooth or exactly zero after all particles have been engulfed by dark halos.

The adhesion model predicts that the dark matter density distribution in voids has a hierarchical cellular structure in which large cells contain cells of smaller sizes, in which there are even smaller cells, and so on, down to the smallest cells, from which the structure formation began (see [95]).

The important question of the fraction of matter in the hierarchy structures remains open. Modern numerical calculations definitely show that the mass fraction decreases quite rapidly with the structure scale, but there is no quantitative answer to this question yet. The mass fraction contained in different elements of the cosmic web [19] mentioned in the introduction is not final. First, definitions of the structure elements in calculations have several parameters, which can change in the future. Second, the definitions themselves are not yet commonly accepted and can be changed. And third, the results depend on the smoothing scale of the initial spectrum used in numerical models, as well as on the size of the region used in simulations.

For example, the structure in paper [19] was modeled in a cube $150 h^{-1}$ Mpc in size, which is about 214 Mpc for the assumed cosmological parameters. In other words, the model region amounts to about 1/50 of the size or 10^{-5} of the volume of the observed Universe. This means that some part of the initial spectrum with waves longer than 214 Mpc is absent in the model, which mostly affects the initial potential, because it depends on the long-wavelength part of the spectrum more strongly than the initial density and velocity perturbations. The adhesion model predicts that the structure

strongly depends on the initial potential, and hence the results of calculations of regions comparable to the size of the Universe can be significantly different.

Nevertheless, the adhesion model, which was proposed about a quarter of a century ago [20, 36, 37], continues developing [43, 82–94, 97] and is now used as an efficient theoretical approach that helps understand and predict specific features of complicated processes, including the formation of galaxies [120–122], interstellar medium turbulence [123], and the large-scale structure of the Universe [21, 22, 31, 40, 41, 124].

This study was supported by the RFBR grant 11-02-00774, the grant of state support of leading scientific schools NSh-3700.2010.2, and the project of the Special Federal Program “Research and Teaching Community of Innovative Russia” (contract No. 02.740.11.0565). The authors acknowledge J Hidding and R Van de Weijgaert, who kindly furnished several new figures for this review.

References

- Zel'dovich Ya B *Astrofiz.* **6** 319 (1970) [*Astrophys. J.* **6** 164 (1970)]
- Zel'dovich Ya B *Astron. Astrophys.* **5** 84 (1970)
- Shandarin S F, Sunyaev R A *Astron. Astrophys.* **500** 19 (2009)
- Shandarin S F, Doroshkevich A G, Zel'dovich Ya B *Usp. Fiz. Nauk* **139** 83 (1983) [*Sov. Phys. Usp.* **26** 46 (1983)]
- Gurevich A V, Zybin K P *Usp. Fiz. Nauk* **165** 723 (1995) [*Sov. Phys. Usp.* **38** 687 (1995)]
- Knop R A et al. (Supernova Cosmology Project) *Astrophys. J.* **598** 102 (2003)
- Riess A G et al. (Supernova Search Team) *Astrophys. J.* **607** 665 (2004)
- Gorbunov D S, Rubakov V A *Vvedenie v Teoriyu Rannei Vseleynoi. Teoriya Goryachego Bol'shogo Vzryva* (Introduction to the Theory of the Early Universe: Hot Big Bang Theory) (Moscow: LKI, 2008) [Translated into English (Singapore: World Scientific, 2011)]
- Mukhanov V *Physical Foundations of Cosmology* (Cambridge: Cambridge Univ. Press, 2005)
- Komatsu E et al. (WMAP Collab.) *Astrophys. J. Suppl.* **180** 330 (2009)
- Percival W J et al. (The 2dFGRS Team) *Mon. Not. R. Astron. Soc.* **337** 1068 (2002)
- Dodelson S et al. (SDSS Collab.) *Astrophys. J.* **572** 140 (2002)
- Freedman W L et al. (HST Collab.) *Astrophys. J.* **553** 47 (2001)
- Lahav O, Liddle A R, The Review of Particle Physics 2010 (aka the Particle Data Book), <http://pdg.lbl.gov/>
- Burduzha V V *Usp. Fiz. Nauk* **180** 439 (2010) [*Phys. Usp.* **53** 419 (2010)]
- Rubakov V A *Usp. Fiz. Nauk* **181** 655 (2011) [*Phys. Usp.* **54** 633 (2011)]
- Navarro J F et al. *Mon. Not. R. Astron. Soc.* **402** 21 (2010)
- Zeldovich Ya B, Einasto J, Shandarin S F *Nature* **300** 407 (1982)
- Aragón-Calvo M A, van de Weygaert R, Jones B J T *Mon. Not. R. Astron. Soc.* **408** 2163 (2010)
- Gurbatov S N, Saichev A I, Shandarin S F *Mon. Not. R. Astron. Soc.* **236** 385 (1989)
- Bond N A, Strauss M A, Cen R *Mon. Not. R. Astron. Soc.* **406** 1609 (2010)
- Bond N A, Strauss M A, Cen R *Mon. Not. R. Astron. Soc.* **409** 156 (2010)
- Friedman A Z. *Phys.* **10** 377 (1922)
- Hubble E *Proc. Natl. Acad. Sci. USA* **15** 168 (1929)
- Geller M J, Huchra J P *Science* **246** 897 (1989)
- Gott J R (III) et al. *Astrophys. J.* **624** 463 (2005)
- Jenkins A et al. (Virgo Consortium) *Astrophys. J.* **499** 20 (1998)
- Zeldovich Ya B, Novikov I D *Stroenie i Evolyutsiya Vseleynoi* (Structure and Evolution of the Universe) (Moscow: Nauka, 1975)
- Peebles P J E *The Large-scale Structure of the Universe* (Princeton, NJ: Princeton Univ. Press, 1980)
- Shandarin S F, Zeldovich Ya B *Rev. Mod. Phys.* **61** 185 (1989)
- Sahni V, Coles P *Phys. Rep.* **262** 1 (1995)
- Jeans J H *Astronomy and Cosmogony* (Cambridge: The Univ. Press, 1928)
- Lifshitz E M *Zh. Eksp. Teor. Fiz.* **16** 587 (1946)
- Doroshkevich A G et al. *Mon. Not. R. Astron. Soc.* **192** 321 (1980)
- Klypin A A, Shandarin S F *Mon. Not. R. Astron. Soc.* **204** 891 (1983)
- Gurbatov S N, Saichev A I *Izv. Vyssh. Uchebn. Zaved. Radiofiz.* **27** 456 (1984) [*Radiophys. Quantum Electron.* **27** 303 (1984)]
- Gurbatov S N, Saichev A I, Shandarin S F *Dokl. Akad. Nauk SSSR* **285** 323 (1985) [*Sov. Phys. Dokl.* **20** 921 (1985)]
- Burgers J M *Kon. Ned. Akad. Wet. Verh.* **17** 1 (1939)
- Burgers J M *The Nonlinear Diffusion Equation* (Dordrecht: D. Reidel, 1974)
- Weinberg D H, Gunn J E *Mon. Not. R. Astron. Soc.* **247** 260 (1990)
- Weinberg D H, Gunn J E *Astrophys. J. Lett.* **352** L25 (1990)
- Gurbatov S N, Malakhov A N, Saichev A I *Nelineinye Sluchainye Volny v Sredakh bez Dispersii* (Nonlinear Random Waves and Turbulence in Nondispersive Media: Waves, Rays, Particles) (Moscow: Nauka, 1990) [Translated into English (Manchester: Manchester Univ. Press, 1991)]
- Vergassola M et al. *Astron. Astrophys.* **289** 325 (1994)
- Molchanov S A, Surgailis D, Woyczynski W A *Ann. Appl. Probab.* **7** 200 (1997)
- Gurbatov S N, Rudenko O V, Saichev A I *Volny i Struktury v Nelineinykh Sredakh bez Dispersii. Prilozheniya k Nelineinoy Akustike* (Waves and Structures in Nonlinear Nondispersive Media: General Theory and Applications to Nonlinear Acoustics) (Moscow: Fizmatlit, 2008) [Translated into English (Berlin: Springer-Verlag jointly with Higher Education Press, 2011)]
- Seljak U, Zaldarriaga M, http://lambda.gsfc.nasa.gov/toolbox/tb_cmbfast_ov.cfm
- Jones B J T *Mon. Not. R. Astron. Soc.* **307** 376 (1999)
- Carroll S M, Press W H, Turner E L *Annu. Rev. Astron. Astrophys.* **30** 499 (1992)
- Shandarin S F *Physica D* **77** 342 (1994)
- Zel'dovich Ya B, Mamaev A V, Shandarin S F *Usp. Fiz. Nauk* **139** 153 (1983) [*Sov. Phys. Usp.* **26** 77 (1983)]
- Doroshkevich A G, Shandarin S F *Astron. Zh.* **55** 1144 (1978) [*Sov. Astron.* **22** 653 (1978)]
- Bardeen J M et al. *Astrophys. J.* **304** 15 (1986)
- Lee J, Shandarin S F *Astrophys. J.* **500** 14 (1998)
- Doroshkevich A G *Astrofiz.* **6** 581 (1970) [*Astrophys. J.* **6** 320 (1970)]
- Arnold V I, Shandarin S F, Zel'dovich Ya B *Geophys. Astrophys. Fluid Dyn.* **20** 111 (1982)
- Shandarin S F et al. *Phys. Rev. Lett.* **75** 7 (1995)
- Shandarin S F *JCAP* (05) 015 (2011)
- Shandarin S F, Habib S, Heitmann K *Phys. Rev. D* **85** 083005 (2012)
- Nusser A, Dekel A *Astrophys. J.* **362** 14 (1990)
- Coles P, Melott A L, Shandarin S F *Mon. Not. R. Astron. Soc.* **260** 765 (1993)
- Melott A L, Pellman T F, Shandarin S F *Mon. Not. R. Astron. Soc.* **269** 626 (1994)
- Beacom J F et al. *Astrophys. J.* **372** 351 (1991)
- Little B, Weinberg D H, Park C *Mon. Not. R. Astron. Soc.* **253** 295 (1991)
- Melott A L, Shandarin S F *Astrophys. J.* **410** 469 (1993)
- Aurell E, Gurbatov S N, Wertgeim I I *Phys. Lett. A* **182** 109 (1993)
- Gurbatov S N, Pasmanik G V *Zh. Eksp. Teor. Fiz.* **115** 564 (1999) [*JETP* **88** 309 (1999)]
- Doroshkevich A G, Ryaben'kii V S, Shandarin S F *Astrofiz.* **9** 257 (1973) [*Astrophys. J.* **9** 144 (1973)]
- Munshi D, Sahni V, Starobinsky A A *Astrophys. J.* **436** 517 (1994)
- Melott A L, Shandarin S F, Weinberg D H *Astrophys. J.* **428** 28 (1994)
- Hidding J et al. *Mon. Not. R. Astron. Soc.* (2011), to be published
- Hidding J et al. *Mon. Not. R. Astron. Soc.* (2012), to be published
- Saichev A I, Woyczynski W A *Distributions in the Physical and Engineering Sciences* Vol. 1 (Boston: Birkhäuser, 1997)
- Saichev A I, Woyczynski W A *IMA Vol. Math. Appl.* **77** 167 (1996)
- Saichev A I, Woyczynski W A *IMA Vol. Math. Appl.* **85** 359 (1997)
- Bernardeau F, Kofman L *Astrophys. J.* **443** 479 (1995)
- Buchert T, Domínguez A *Astron. Astrophys.* **438** 443 (2005)
- Weinan E, Rykov Yu G, Sinai Ya G *Commun. Math. Phys.* **177** 349 (1996)

78. Andrievsky A A, Gurbatov S N, Sobolevsky A N *Zh. Eksp. Teor. Fiz.* **131** 1018 (2007) [*JETP* **104** 887 (2007)]
79. Shandarin S F, Sathyaprakash B S *Astrophys. J.* **467** L25 (1996)
80. Hopf E *Commun. Pure Appl. Math.* **3** 201 (1950)
81. Cole J D *Quart. Appl. Math.* **9** 225 (1951)
82. Aurell E et al. *Physica D* **186** 171 (2003)
83. Noullez A, Fanelli D, Aurell E *J. Comput. Phys.* **186** 697 (2003); cond-mat/0101336
84. Fanelli D, Aurell E, Noullez A, in *Astrophysical Supercomputing using Particle Simulations* (IAU Symp., No. 208, Eds J Makino, P Hut) (San Francisco: Astronomical Society of the Pacific, 2003) p. 389
85. Fanelli D, Aurell E *Astron. Astrophys.* **395** 399 (2002)
86. Gurbatov S N, in *Dark Matter in the Universe. Proc. of the Intern. School of Physics E. Fermi, Course CXXXII* (Eds S Bonometto, J R Primack, A Provenzale) (Oxford: IOS Press, 1996) p. 645
87. Kofman L, Pogosian D, Shandarin S *Mon. Not. R. Astron. Soc.* **242** 200 (1990)
88. Kofman L et al. *Astrophys. J.* **393** 437 (1992)
89. Sahni V, Sathyaprakash B S, Shandarin S F *Astrophys. J.* **431** 20 (1994)
90. Arnold V I, Baryshnikov Yu M, Bogayevsky I A, in Gurbatov S N, Rudenko O V, Saichev A I *Waves and Structures in Nonlinear Nondispersive Media: General Theory and Applications to Nonlinear Acoustics* (Berlin: Springer-Verlag jointly with Higher Education Press, 2011) p. 290
91. Saichev A I, Woyczynski W A *SIAM J. Appl. Math.* **56** 1008 (1996)
92. Bernardeau F, Valageas P *Phys. Rev. D* **81** 043516 (2010)
93. Bernardeau F, Valageas P *Phys. Rev. E* **82** 016311 (2010)
94. Valageas P, Bernardeau F *Phys. Rev. D* **83** 043508 (2011)
95. Hidding J “Adhesion: a sticky way of understanding Large Scale Structure”, MS Thesis (Groningen, The Netherlands: Univ. of Groningen, 2010); <http://www.astro.rug.nl/~hidding/go/report.pdf>
96. Bogaevsky I A, math-ph/0407073
97. Khanin K, Sobolevski A *Phil. Trans. R. Soc. London A* **368** 1579 (2010); arXiv:1001.0498
98. Bogaevskii I A *Mat. Sb.* **197** (12) 11 (2006) [*Sb. Math.* **197** 1723 (2006)]
99. Brézis H, in *Opérateurs Maximaux Monotones et Semi-groupes de Contractions dans les Espaces de Hilbert* (North-Holland Mathematical Studies, 5) (Amsterdam: North-Holland Publ., 1973)
100. Cannarsa P, Sinestrari C *Semiconcave Functions, Hamilton-Jacobi Equations, and Optimal Control* (Progress in Nonlinear Differential Equations and Their Applications, Vol. 58) (Boston: Birkhäuser, 2004)
101. Bec J, Khanin K *Phys. Rep.* **447** 1 (2007)
102. Barabási A-L, Stanley H E *Fractal Concepts in Surface Growth* (Cambridge: Cambridge Univ. Press, 1995)
103. Kardar M, Parisi G, Zhang Y-C *Phys. Rev. Lett.* **56** 889 (1986)
104. Bouchaud J P, Mézard M, Parisi G *Phys. Rev. E* **52** 3656 (1995)
105. Woyczynski W A *Burgers-KPZ Turbulence. Gottingen Lectures* (Berlin: Springer, 1998)
106. Alberverio S, Molchanov S A, Surgailis D *Probab. Theory Relat. Fields* **100** 457 (1994)
107. Gurbatov S N *Phys. Rev. E* **61** 2595 (2000)
108. Rudenko O V, Soluyan S I *Teoreticheskie Osnovy Nelineinoy Akustiki* (Theoretical Foundation of Nonlinear Acoustics) (Moscow: Nauka, 1975) [Translated into English (New York: Consultants Bureau, 1977)]
109. Gurbatov S N, Saichev A I, Yakushkin I G *Usp. Fiz. Nauk* **141** 221 (1983) [*Sov. Phys. Usp.* **26** 857 (1983)]
110. Rudenko O V *Usp. Fiz. Nauk* **149** 413 (1986) [*Sov. Phys. Usp.* **29** 620 (1986)]
111. Frachebourg L, Martin Ph A J *J. Fluid Mech.* **417** 323 (2000)
112. Frisch U *Turbulence: the Legacy of A N Kolmogorov* (Cambridge: Cambridge Univ. Press, 1995) [Translated into Russian (Moscow: FAZIS, 1998)]
113. Gurbatov S N, Saichev A I *Zh. Eksp. Teor. Fiz.* **80** 689 (1981) [*Sov. Phys. JETP* **53** 347 (1981)]
114. Gurbatov S et al. *J. Fluid Mech.* **344** 349 (1997)
115. Gurbatov S, Moshkov A Yu, Noullez A *Phys. Rev. E* **81** 046312 (2010)
116. Saichev A I, Woyczynski W A *J. Fluid Mech.* **331** 313 (1997)
117. Shandarin S F, arXiv:0912.4520
118. Kofman L A, Shandarin S F *Nature* **334** 129 (1988)
119. Diemand J, Moore B, Stadel J *Nature* **433** 389 (2005)
120. Domínguez-Tenreiro R et al. *Mon. Not. R. Astron. Soc.* **413** 3022 (2011)
121. Oñorbe J et al. *Astrophys. J.* **732** L32 (2011)
122. Pichon C et al. *Mon. Not. R. Astron. Soc.* **418** 2493 (2011); arXiv:1105.0210
123. Zhu W, Feng L-L, Fang L-Z *Mon. Not. R. Astron. Soc.* **415** 1093 (2011)
124. Orban C, Weinberg D H *Phys. Rev. D* **84** 063501 (2011)